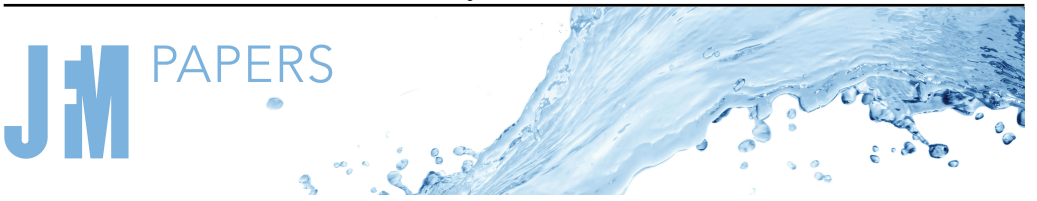
J. Fluid Mech. (2026), *vol.* 1040, A48, doi:10.1017/jfm.2026.11898



Finger dynamics in rarefaction-driven single-mode Rayleigh–Taylor instability under high-amplitude conditions

Zhigang Zhai[1], **Yue Li**[1], **Xing Gao**[1] and **Xu Guo**[1]

[1]State Key Laboratory of High-Temperature Gas Dynamics, School of Engineering Science, University of Science and Technology of China, Hefei 230026, PR China

Corresponding author: Xu Guo, clguoxu@ustc.edu.cn

(Received 4 December 2025 UTC; revised 3 June 2026 UTC; accepted 6 July 2026 UTC)

This study examines the finger dynamics of high-amplitude, single-mode rarefaction-driven Rayleigh–Taylor instability (RTI) through rarefaction-tube experiments and numerical simulations. Unlike RTI driven by gravity or mechanical acceleration, rarefaction-driven RTI features a distinct wavefront-traversal (WT) stage prior to the linear stage. During the WT stage, finger velocities are decomposed into contributions from the rarefaction flow's bulk motion and baroclinic-vorticity-induced velocity, and a theoretical framework is developed to quantitatively evaluate these components. Incorporating the WT-stage outcomes into the Layzer-type model (Li *et al.* 2025 *J. Fluid Mech.* 1016, A27) resolves the singularity-induced ill posedness at high amplitudes and, with the inclusion of interface stretching, enables accurate prediction of perturbation growth up to the quasi-steady stage. At high amplitudes, the inertial effect provides the fundamental contribution to bubble growth, whereas the curvature effect governs the transition to the quasi-steady state and the stretching effect determines the magnitude of the quasi-steady velocity. Beyond the quasi-steady stage, pronounced bubble deceleration emerges due to strong vorticity transport from the bubble region toward the spike. This transport reduces the interfacial vorticity that sustains bubble motion and thereby results in growth suppression. As the vortices shed from the spike reach the vicinity of the bubble tip, their induced velocity becomes significant, eventually terminating the deceleration and leading to a fluctuating saturated state.

Key words: gas dynamics

© The Author(s), 2026. Published by Cambridge University Press.

https://doi.org/10.1017/jfm.2026.11898 Published online by Cambridge University Press

1. Introduction

When two fluids of different densities, separated by a perturbed interface, are continuously accelerated from the less dense to the denser one, vorticity is baroclinically deposited by the misalignment between local pressure and density gradients. The vorticity drives sustained growth of interface perturbations, known as Rayleigh–Taylor instability (RTI) (Rayleigh 1883; Taylor 1950). Generally, RTI begins with a linear stage characterised by exponential growth, followed by a nonlinear stage where large-scale finger structures of bubbles (light fluids penetrating heavy fluids) and spikes (heavy fluids penetrating light fluids) emerge. During the early nonlinear stage, referred to as the quasi-steady phase, these finger structures maintain nearly constant velocities, whereas in the highly nonlinear stage, bubbles may reaccelerate beyond potential-flow predictions (Ramaprabhu *et al.* 2006; Yan *et al.* 2016; Fu *et al.* 2023; Liu *et al.* 2025). As the evolution progresses, the interface structures span a wide range of scales, eventually transitioning into a turbulent mixing regime. The RTI plays a crucial role in diverse natural phenomena and engineering applications, such as supernova explosions (Kuranz *et al.* 2018), inertial confinement fusion (ICF) (Qiao & Lan 2021; Zhang *et al.* 2024; Yan *et al.* 2025), scramjet engines (Li & Book 1991; Urzay 2018) and various topics in planetary geophysics (Pouquet & Mininni 2014; Ravid *et al.* 2021). Several comprehensive reviews have highlighted the significance of RTI in these contexts (Abarzhi & Sreenivasan 2010; Boffetta & Mazzino 2017; Zhou 2017*a*,*b*; Zhou *et al.* 2019, 2021, 2025; Banerjee 2020; Livescu 2020).

The RTI can be triggered by various acceleration mechanisms, typically by gravity. In a gravitational field, the interface between a heavy fluid placed above a lighter one becomes unstable, and numerous experiments have examined RTI evolution under this constant acceleration (Jacobs & Dalziel 2005; Banerjee & Andrews 2006; Huang *et al.* 2007; Andrews & Dalziel 2010; Banerjee *et al.* 2010; White *et al.* 2010; Lawrie & Dalziel 2011; Akula *et al.* 2017; Liang *et al.* 2024). To study RTI under non-uniform driving conditions, mechanical systems such as rocket rigs (Read 1984; Youngs 1989), gas guns (Kucherenko *et al.* 1997, 2003) and linear electric motors (Dimonte *et al.* 1996; Dimonte & Schneider 2000) have been employed to produce time-varying accelerations ranging from 10^1 to 10^2 times the gravitational acceleration (g_0). Unlike RTI driven by constant or variable acceleration, rarefaction-driven RTI occurs in a flow where both the acceleration and density evolve with time, owing to the continuous decay of wave strength from wave front to tail (Gao *et al.* 2024). In addition, rarefaction-tube experiments can reach interface accelerations of the order of $10^4 g_0$ (Morgan *et al.* 2018; Li *et al.* 2025), far exceeding those produced by conventional mechanical drivers. Previous studies (Gao *et al.* 2024) have shown that rarefaction-induced flow acceleration exhibits a power-law behaviour. Such acceleration fields possess self-similar scaling properties that may help reveal the essential physics governing unstable mixing (Abarzhi 2024).

In practical applications, rarefaction-driven RTI also plays an important role. In ICF, the laser-driven shock propagates inward and hits the ablator/fuel interface, forming a rarefaction wave that propagates back toward the ablation front. The interaction between the rarefaction wave and the ablation front triggers RTI growth, leading to mixing between the ablator material and fuel and thereby degrading the fusion yield (Goncharov *et al.* 2000; Qiao & Lan 2021). In scramjet engines, rarefaction waves generated by geometric corners or fuel injection interact with the fuel/oxidiser interface, enhancing mixing and thus improving combustion efficiency (Li & Book 1991; Li *et al.* 1991; Zhou 2017*a*). As a result, it is essential and critical to explore the evolution characteristics of rarefaction-driven RTI.

https://doi.org/10.1017/jfm.2026.11898 Published online by Cambridge University Press

Since Taylor (1950) formulated the linear stability theory for RTI under constant acceleration, finger growth in the linear stage has been well understood; however, describing the nonlinear evolution of RTI fingers remains challenging. Layzer (1955) first proposed a model to predict the asymptotic growth of bubbles in the quasi-steady stage under conditions of constant acceleration, zero initial amplitude ($\eta_0 = 0$) and a fluid–vacuum interface ($A_0 = 1$), where $A_0 = (\rho_{L0} - \rho_{R0})/(\rho_{L0} + \rho_{R0})$ is the initial Atwood number, with ρ_{L0} and ρ_{R0} being the densities of the fluids on the two sides of the interface. Mikaelian (1998) and Zhang (1998) extended Layzer's model to non-zero η_0, with the former deriving the asymptotic growth rate for bubbles and the latter for spikes. Further extensions to asymptotic bubble growth at arbitrary A_0 were achieved by Goncharov (2002) and Sohn (2003) using different velocity potentials. Recent theoretical advancements have addressed the asymptotic growths of both bubbles and spikes at arbitrary A_0 (Zhang & Guo 2016; Guo & Zhang 2020; Liu *et al.* 2023*b*). Layzer's potential-flow framework has also been adapted to account for bubble growth under time-varying acceleration (Mikaelian 2014; Ramaprabhu *et al.* 2016), and further extended to more complex scenarios involving time-dependent acceleration and variable density – specifically, for bubbles by Mikaelian (2009), and for both bubbles and spikes by Li *et al.* (2025). In addition, the extension of Layzer's model to magnetohydrodynamics enables analytical predictions of asymptotic bubble and spike growth rates at arbitrary A_0 (Gréa & Briard 2023). Beyond Layzer-type potential-flow models, major advances in nonlinear RTI theory have also been achieved through the group-theory framework developed by Abarzhi and collaborators (Abarzhi *et al.* 2003*a*; Abarzhi *et al.* 2003*b*; Abarzhi *et al.* 2015; Abarzhi *et al.* 2019*a*,*b*, 2023; Meshkov & Abarzhi 2019; Chan *et al.* 2023; Abarzhi 2024), which exploits the symmetries of the flow to describe the coherent nonlinear finger dynamics. Overall, these theoretical approaches demonstrate robust predictive capability for low-amplitude RTI finger growth within their respective applicability ranges. Although the derivations of these theoretical models do not explicitly require low initial amplitudes (typically $\eta_0/\lambda < 0.1$, where λ is the wavelength), the evolution of finger curvature at relatively high amplitudes may lead to singularities, rendering the model mathematically invalid (Mikaelian 2008). Therefore, the prediction of finger growth in high-amplitude RTI remains challenging, especially for rarefaction-driven RTI with unsteady acceleration and density fields.

Previous studies have shown that potential-flow models fail to capture the late-time dynamics of low-amplitude RTI, as bubble re-acceleration disrupts the quasi-steady evolution. This re-acceleration was numerically reported in RTI driven by gravity at low and moderate A_0 (<0.6) and attributed to secondary Kelvin–Helmholtz (KH) vortices that induce an additional upward velocity (Ramaprabhu *et al.* 2006, 2012). In ablative RTI, Betti & Sanz (2006) attributed the re-acceleration to vorticity convection: vortices generated near the spike are convected toward the bubble tip by the plasma flowing into the bubble, and these vortices exert centrifugal forces on the bubble tip, driving its re-acceleration. Following this interpretation, Wei & Livescu (2012) and Bian *et al.* (2020) conducted simulations across a broad parameter space ($A_0 = 0.04$–0.80 and the perturbation Reynolds numbers $Re_p = 100$–$20\,000$) to investigate the dependence of re-acceleration on initial conditions. Their results showed that increasing Re_p promotes re-acceleration, while increasing A_0 tends to maintain the quasi-steady state. At $A_0 = 0.80$ and Re_p up to 20 000, Bian *et al.* (2020) reported the absence of re-acceleration, as at such high A_0, the spike grows much faster than the bubble, shifting the region of strongest vorticity generation downward toward the spike. Consequently, the vortices must travel a longer distance to reach the bubble tip, during which their strength dissipates, preventing the bubble from re-accelerating. Recent rarefaction-driven RTI experiments at $A_0 = 0.85$

https://doi.org/10.1017/jfm.2026.11898 Published online by Cambridge University Press

and $Re_p \sim 30\,000$ also reported that the bubble velocity asymptotically approaches saturation instead of re-acceleration (Li *et al.* 2025). Note that these studies of finger dynamics have primarily focused on low-amplitude interfaces. Under high-amplitude conditions ($\eta_0/\lambda > 0.1$), the interface may rapidly transition into the quasi-steady phase, resulting in enhanced spike–bubble asymmetry and accelerated nonlinear development. However, the corresponding finger dynamics under such conditions remains poorly understood.

In addition, in gravity- or mechanically driven RTI, acceleration is applied instantaneously to the entire perturbed interface, such that the perturbation growth directly enters the linear stage. In contrast, rarefaction-driven RTI features a gradual imposition of acceleration from upstream to downstream, as the rarefaction wavefront sweeps across the interface. This leads to a distinct wavefront-traversal (WT) stage that precedes the linear stage in rarefaction-driven RTI. Moreover, a higher initial amplitude prolongs the WT stage. The extended duration enhances baroclinic vorticity deposition and promotes interface stretching (Cong *et al.* 2022). Nevertheless, the perturbation growth dynamics during the WT stage and its impact on subsequent evolution remain unclear.

In summary, despite extensive studies on RTI, several key issues remain unresolved for rarefaction-driven RTI under high-amplitude conditions. These include a quantitative assessment of perturbation evolution during the WT stage, a clear understanding of how its late-time behaviour differs from that in low-amplitude cases, and the development of accurate models for finger growth. To address these questions, the present study investigates rarefaction-driven RTI at high-amplitude, single-mode interfaces through rarefaction-tube experiments. An improved soap-film technique is developed to generate well-defined single-mode perturbations with η_0/λ ranging from 0.1 to 0.5, far exceeding the values (<0.1) in previous RTI studies. Theoretical models are formulated to predict finger growth through the WT, linear-to-weakly nonlinear and quasi-steady stages, and numerical simulations are performed in conjunction with experiments to elucidate the finger evolution beyond the quasi-steady stage.

2. Experimental methods

The soap-film technique (Liu *et al.* 2018; Li *et al.* 2023) is further refined in this study to enable the generation of high-amplitude single-mode interfaces. As shown in figure 1(*a*), the interface formation device comprises two transparent acrylic sub-devices, A and B, whose contacting edges are machined into sinusoidal profiles. In previous studies (Li *et al.* 2025), a super-hydrophobic-oleophobic (SHO) coating was applied along these edges to constrain the soap film and generate low-amplitude interfaces. However, for higher amplitudes, the SHO coating alone does not provide sufficient confinement. To enhance confinement, sinusoidal constraint strips are additionally attached to the edges of sub-device A. These strips protrude less than 0.3 mm into the flow region and exert negligible influence on interface evolution (Wang *et al.* 2022). A well-defined two-dimensional (2-D) single-mode interface is then formed by drawing a rectangular brush dipped in soap solution along the sinusoidal edge (figure 1*b*). In the present study, the interface wavelength is fixed at $\lambda = 40$ mm. Five high-amplitude single-mode perturbations are generated, with $\eta_0 = 4,\ 8,\ 12,\ 16$ and 20 mm, corresponding to $\eta_0/\lambda = 0.1, 0.2, 0.3, 0.4$ and 0.5. For comparison, a low-amplitude case ($\eta_0 = 2$ mm, $\lambda = 40$ mm) from our previous work (Li *et al.* 2025) is also included. The corresponding initial interface parameters for all cases are summarised in table 1.

Sub-devices A and B are assembled using a drawer-type mechanism and inserted into the test section of a horizontal rarefaction tube (figure 1*c*), and the centre of the initial

https://doi.org/10.1017/jfm.2026.11898 Published online by Cambridge University Press

Case	η_0 (mm)	λ (mm)	η_0/λ
2-40	2	40	0.05
4-40	4	40	0.1
8-40	8	40	0.2
12-40	12	40	0.3
16-40	16	40	0.4
20-40	20	40	0.5

Table 1. Initial interface parameters for different cases. Here, η_0 and λ represent the initial amplitude and wavelength, respectively.

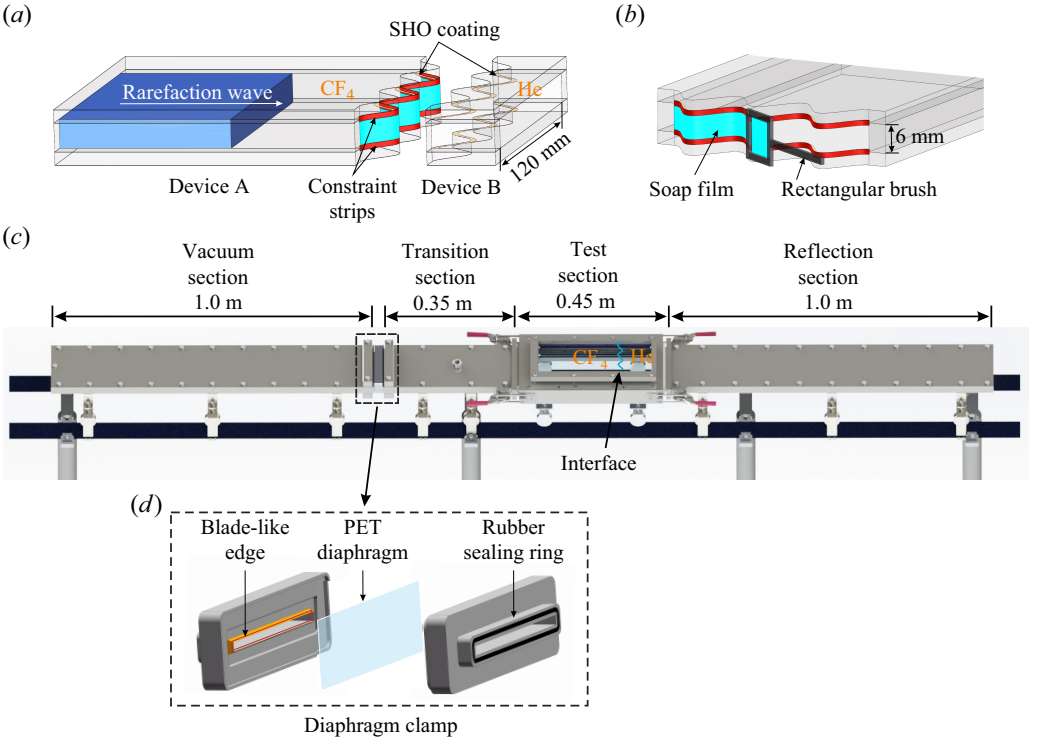


Figure 1. Schematics of the experimental apparatus: the interface formation device (*a*,*b*), the horizontal rarefaction tube (*c*) and the diaphragm clamp (*d*). The SHO coating, works in conjunction with the constraint strips to confine the soap film into high-amplitude single-mode perturbations. Panels (*c*) and (*d*) are adapted from Li *et al.* 2025 *J. Fluid Mech.* **1016**, A27, with permission from Cambridge University Press.

interface is located 758.5 mm downstream of the diaphragm separating the vacuum and transition sections. Note that, in rarefaction-driven flows, the densities on both sides of the interface decrease continuously, causing the interface to become increasingly indistinct in experimental schlieren imaging at late times (Guo *et al.* 2025; Zhai *et al.* 2025). Therefore, two gases with a large density contrast are required to achieve a high A_0 for clear observation. Here, CF_4 and helium are selected and injected into the test section through inlet holes in the transition and reflection sections, respectively. These two gases are separated by the soap film, forming a sharp initial interface. To ensure reproducible initial conditions, the inflation rate is controlled by flow valves, yielding

https://doi.org/10.1017/jfm.2026.11898 Published online by Cambridge University Press

A_0	Heavy fluid	Light fluid	p_{vac}	p_{other}
0.85	90 % CF_4 + 10 % Air	90 % Helium + 10 % Air	10 kPa	101 kPa

Table 2. Initial experimental parameters and settings for different cases. Here, A_0 is the initial Atwood number and p_{vac} and p_{other} denote the pressures within the vacuum and other sections at the diaphragm-rupture time, respectively.

uniform gas concentrations across runs. The resulting volume fractions of CF_4 and helium are each approximately 90 %, corresponding to $A_0 = 0.85$ (see table 2 for detailed gas compositions). This value matches that used in previous low-amplitude RTI experiments (Li *et al.* 2025), allowing a direct comparison.

As shown in figure 1(*c*), the rarefaction tube used in the experiments comprises a 1.0 m vacuum section, a 0.35 m transition section, a 0.45 m test section and a 1.0 m reflection section (Gao *et al.* 2024). Both the vacuum and reflection sections are sufficiently long to avoid the influence of end-wall reflections on interface evolution over the experimental duration. The vacuum and transition sections are separated by a 3 μm-thick polyethylene terephthalate (PET) diaphragm, which is secured by a specially designed clamp device. As shown in figure 1(*d*), the clamp device consists of two sub-devices, and the left one is equipped with a sharp blade-like edge. Initially, the pressure throughout the rarefaction tube is atmospheric ($\sim$ 101 kPa). Air is then evacuated from the vacuum section using a vacuum pump. As the pressure in the vacuum section decreases, the PET diaphragm gradually protrudes toward the low-pressure region. When the pressure in the vacuum section is reduced to approximately 10 kPa, the PET diaphragm ruptures abruptly and is completely severed by the clamp's sharp edge. This process generates a rarefaction wave that propagates downstream into the transition section. The rarefaction wave then arrives at the test section and interacts with the interface, triggering RTI evolution. To ensure that the interface evolution occurs entirely within the rarefaction region, the rarefaction tail should propagate upstream. Previous studies (Li *et al.* 2025) have shown that, under the present experimental conditions, if the pressure ratio p_2/p_1 (where p_2 and p_1 denote the pressures in the transition and vacuum sections at rupture time, respectively) exceeds 5.969, the rarefaction tail propagates upstream. In this work, $p_2/p_1 \approx 10$, satisfying this condition.

The observation window of the test section has a size of 350 × 120 mm^2, and the entire window is captured during the measurements. The flow field within this window is illuminated by a xenon light source (CEL-HXF300, 50 W radiant output) and recorded using a schlieren system combined with a high-speed camera (FASTCAM SA5, Photron Limited) (Guo *et al.* 2022). The camera operates at 30 000 frames per second with an exposure time of 1 μs, providing sufficient temporal resolution for both the instability growth rate ($<$20 m s^{-1}) and the interface velocity ($<$150 m s^{-1}). With a spatial resolution of 0.406 mm pixel^{-1}, the schlieren system can effectively resolve the interface mixing width, which maintains a minimum streamwise extent exceeding 4 mm. The ambient pressure and temperature are approximately 101 kPa and 293.5 K, respectively.

3. Results and discussion

3.1. *One-dimensional rarefaction-driven flow*

Figure 2(*a–c*) shows the one-dimensional (1-D) flow-field distributions within the rarefaction tube before and after the diaphragm rupture. The spatial and temporal origins are defined as the diaphragm position and its rupture time, respectively. As shown in

https://doi.org/10.1017/jfm.2026.11898 Published online by Cambridge University Press

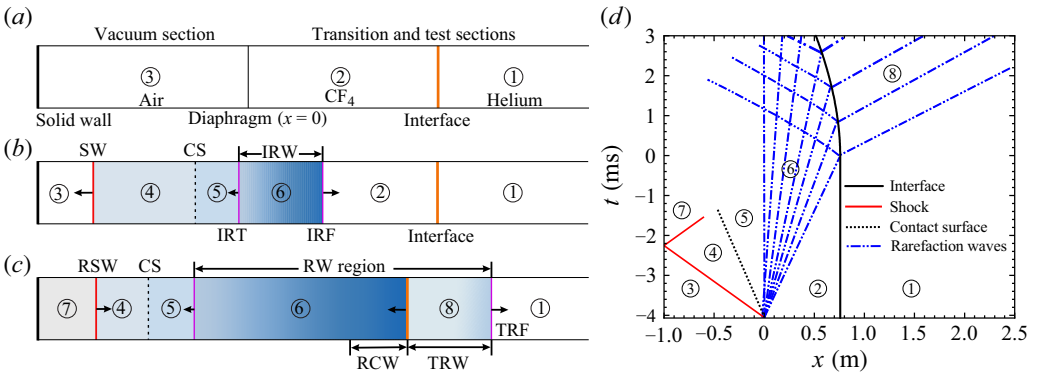


Figure 2. Distributions of the flow field within the rarefaction tube (a) before and (b,c) after the diaphragm rupture; (d) the x–t plot of the 1-D rarefaction-tube flow. IRF and IRT, incident rarefaction wavefront and tail; RSW, reflected shock wave; TRF, transmitted rarefaction wavefront. This figure is adapted from Li *et al.* 2025 *J. Fluid Mech.* **1016**, A27, with permission from Cambridge University Press.

figure 2(a), prior to rupture, the diaphragm and the interface divide the rarefaction tube into regions 1, 2 and 3 from right to left. After the diaphragm ruptures, an incident rarefaction wave (IRW) propagating downstream and a shock wave (SW) propagating upstream are generated, as depicted in figure 2(b). A contact surface (CS) forms between the rarefaction and SWs, and the regions on either side of CS are denoted as regions 4 and 5. As the IRW moves downstream, region 2 is transformed into region 6, in which the flow parameters vary with time. Subsequently, as shown in figure 2(c), the IRW interacts with the CF_4/Helium interface, producing a transmitted rarefaction wave (TRW) and a reflected compression wave (RCW), while the interface is gradually accelerated upstream. Figure 2(d) shows the x–t plot of the waves and the interface within the rarefaction tube, obtained from 1-D gas dynamics theories (Han & Yin 1993). Due to the continuous acceleration induced by the rarefaction wave, the interface exhibits a variable velocity motion. During the experimental time ($t \approx 0$–3 ms), the reflected shock from the end wall does not reach the interface, thereby having no influence on its evolution.

Recently, Gao *et al.* (2024) derived analytic expressions for the 1-D interface acceleration, $g(t)$, and for the fluid densities on either side of the interface, $\rho_R(t)$ and $\rho_L(t)$, in rarefaction-driven flows, where the subscripts 'R' and 'L' denote the right- and left-hand side fluids, respectively. The quantities $g(t)$, $\rho_R(t)$ and $\rho_L(t)$ are calculated using (3.36), (3.34a) and (3.34b), which will also be introduced in § 3.3. The time-dependent Atwood number is defined as $A(t) = [\rho_L(t) - \rho_R(t)]/[\rho_L(t) + \rho_R(t)]$. Figure 3 compares the temporal evolution of the acceleration, fluid densities and Atwood number for a CF_4/helium interface predicted by the theory of Gao *et al.* (2024) with numerical simulations (see Appendix A for details of the numerical method). As shown in figure 3(a), the acceleration initially reaches approximately 6000 g_0 and then decreases with time. As shown in figure 3(b), the densities of both fluids also decrease over time, with the right-hand side fluid exhibiting a more rapid decay, whereas the Atwood number varies only slightly throughout the evolution. Overall, good agreement is observed between the theoretical predictions and numerical results.

3.2. *Interface evolution*

Figure 4(a–e) shows the rarefaction-driven evolution of single-mode interfaces under different high-amplitude conditions. For clarity, the time axes in figure 4(a–e) are

https://doi.org/10.1017/jfm.2026.11898 Published online by Cambridge University Press

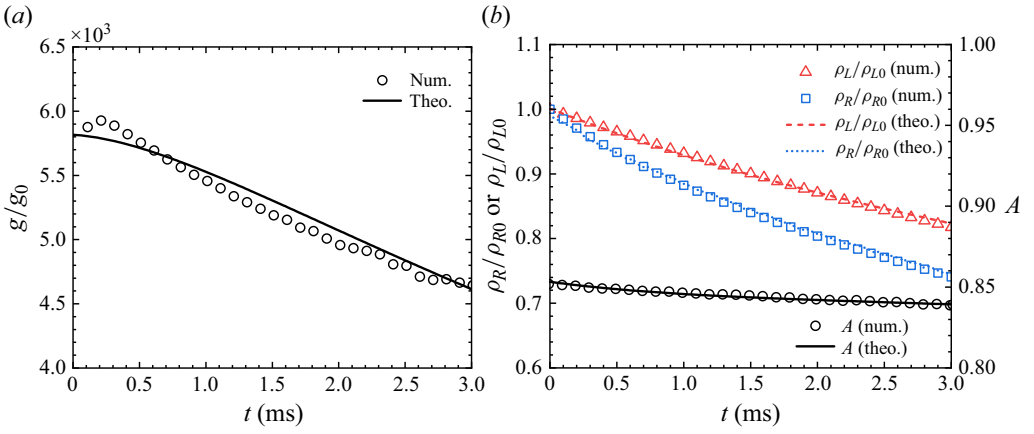


Figure 3. Comparison of the temporal evolution of (*a*) 1-D interface acceleration, and (*b*) fluid densities and Atwood number in rarefaction-driven flows, between simulations and theory. The theoretical line for the interface acceleration $g(t)$ is obtained from (3.36), while those for the densities of fluids on the right (He) and left (CF_4) sides of the interface, $\rho_R(t)$ and $\rho_L(t)$, are given by (3.34*a*) and (3.34*b*), respectively. Here, g_0 denotes the gravitational acceleration, and ρ_{R0} and ρ_{L0} denote the initial densities of fluids on the right and left sides, respectively.

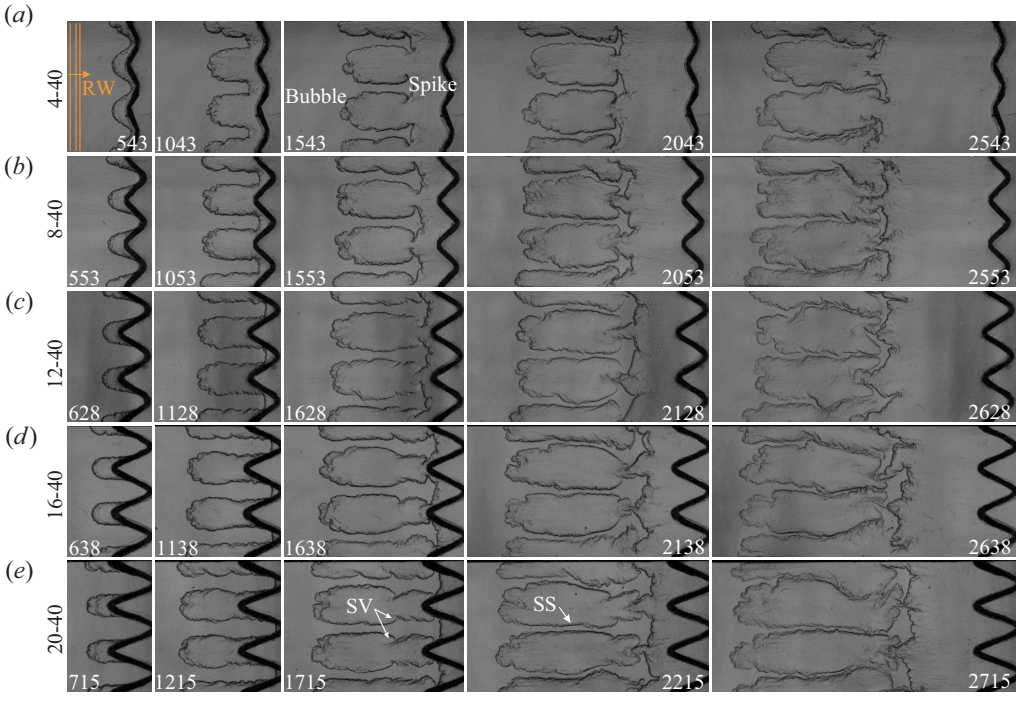


Figure 4. Schlieren images of rarefaction-induced evolution for high-amplitude single-mode interfaces. Here, 'RW' denotes the rarefaction wave, 'SV' denotes the secondary vortices and 'SS' denotes the spike stem. Numbers denote time in μs.

https://doi.org/10.1017/jfm.2026.11898 Published online by Cambridge University Press

shifted by t_{L0}, the travel time of the rarefaction wavefront from the diaphragm to the upstream edge of the interface. Notably, the rarefaction wave is not visible in schlieren observations due to the low density gradient within the rarefaction region. For case 4-40, as shown in figure 4(a), the interface gradually moves upstream due to the rarefaction acceleration, and the interface maintains an approximately sinusoidal shape at early times (543 μs). As the evolution proceeds, the interface becomes increasingly asymmetric and develops pronounced bubble and spike structures, with the formation of a roll-up vortex pair at the spike tip (1043–1543 μs). The bubble expands laterally, while the spike is stretched along the flow direction, leading to a highly elongated spike stem at late times (2043–2543 μs). Secondary instabilities emerge along the interface, characterised by small vortical structures appearing on both the spike stem and the bubble head. These features are markedly more prominent than in previous RTI experiments involving continuous interfaces (Morgan *et al.* 2016, 2018), where a thick diffusive layer suppresses vortex formation.

As η_0/λ increases, the upstream side of the interface initiates movement increasingly earlier than the downstream side. In cases 16-40 and 20-40, this asymmetry even results in the formation of bubbles at early times, while the downstream side remains nearly stationary (638 and 715 μs). As time progresses, secondary instabilities characterised by rolled-up vortical structures develop at the spike tip. Moreover, in addition to the primary vortices near the spike tip, secondary vortices emerge around the midsection of the spike stem, particularly in cases 16-40 and 20-40 (1638 and 1715 μs). These vortices appear to divide the spike into two distinct segments: a thinner left section and a thicker right section. As the secondary vortices gradually move toward the spike head, the stem transitions into a more uniformly slender structure (2638 and 2715 μs).

3.3. *Perturbation growth*

3.3.1. *Wavefront-traversal stage*

The interval between the arrival of the IRF at the upstream interface edge and its departure from the downstream edge is defined as the WT stage. During this stage, the finger-tip velocities can be decoupled into two components: (i) the bulk (background) velocity induced by the rarefaction wave, and (ii) the velocity induced by the vorticity deposited along the interface. To illustrate these two contributions, the numerical pressure and vorticity fields for case 20-40 during the WT stage are presented in figures 5(a–d) and 5(e–h), respectively. For brevity, the upstream and downstream interface edges are hereafter referred to as the bubble and spike tips.

As shown in figure 5(a), when the IRF reaches the bubble tip of the interface ($t = t_{L0}$), the bubble tip acquires a bulk velocity u_b^{bulk}, and begins to move upstream. Subsequently, the rarefaction wave transmits into helium and becomes perturbed due to the interface modulation (figure 5b). Since the rarefaction wavefront propagates at the local sound speed of the fluid ahead, the TRF in He travels faster than the IRF in CF_4 owing to the higher sound speed in helium. As a result, the TRF reaches the spike tip earlier and imparts a bulk velocity, u_s^{bulk}, to the spike tip. As the TRF propagates away from the interface, the interface-induced perturbation progressively weakens, and the wavefront gradually recovers an approximately planar shape (figure 5c). As shown in figure 5(d), when the IRF arrives at the spike tip (the arrival time is defined as t_{R0}), the entire interface becomes fully immersed in the rarefaction region, marking the end of the WT stage. The duration of this stage is therefore given by $\Delta t_{WT} = t_{R0} - t_{L0}$, and the corresponding values for different cases are summarised in table 3.

https://doi.org/10.1017/jfm.2026.11898 Published online by Cambridge University Press

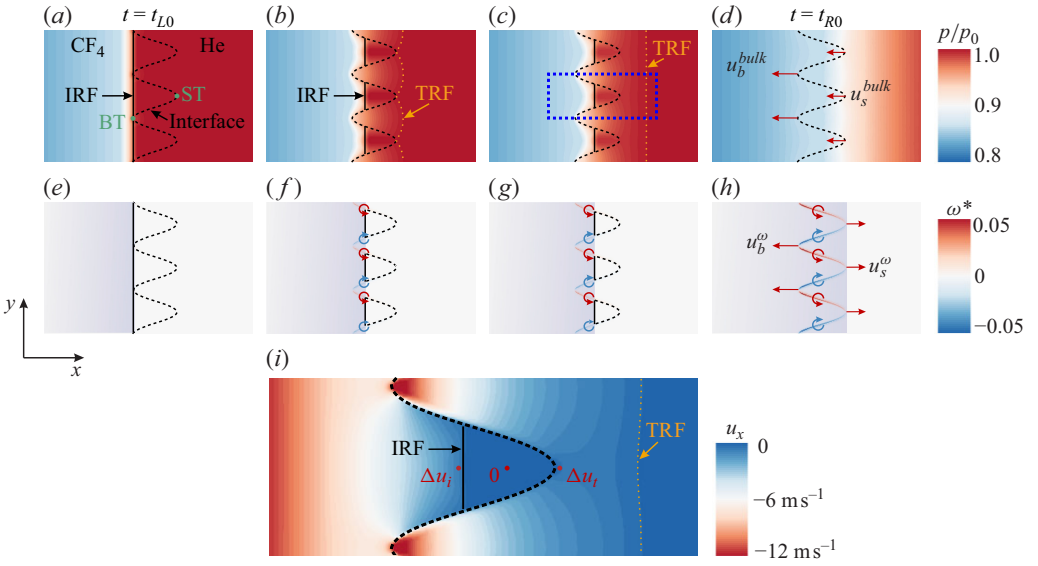


Figure 5. Numerical pressure (*a–d*) and vorticity fields (*e–h*) for a rarefaction-driven single-mode interface during the WT stage. Panels (*a*,*e*) show the instant $t = t_{L0}$ when the IRF reaches the bubble tip (BT); panels (*b*, *f*) depict the moment when the TRF reaches the spike tip (ST); panels (*c*,*g*) show that TRF passes over ST; and panels (*d*,*h*) show the instant $t = t_{R0}$ when IRF reaches ST. Here, u_b^{bulk} (u_s^{bulk}) and u_b^{ω} (u_s^{ω}) denote the bulk and vorticity-induced velocities at the bubble (spike) tip, with red arrows indicating their directions, p is the instantaneous pressure and $\omega^* = (\partial_x u_y - \partial_y u_x)/\sqrt{p_0/\rho_0}$ denotes the dimensionless vorticity, where u_x and u_y are the velocity components in the x- and y-directions, respectively. The reference pressure p_0 and density ρ_0 are taken as the atmospheric pressure (101 kPa) and the air density at room temperature (1.204 kg m^{-3}), respectively. Panel (*i*) presents an enlarged view of the streamwise velocity field corresponding to the region enclosed by the blue dotted line in panel (*c*). Here, Δu_i denotes the velocity increment immediately behind the IRF relative to the value (i.e. zero) ahead of it, and Δu_t denotes the velocity increment immediately downstream of the ST, i.e. the velocity increment relative to the pre-TRF state.

As illustrated in figure 5(*e–h*), baroclinic vorticity is deposited along the interface as the IRF sweeps across the interface from upstream to downstream. Owing to the spatial and temporal variation of both the wave strength and the local interface slope in the single-mode configuration, this deposition process is inherently non-uniform. As a result, vorticity preferentially accumulates near the bubble region, leading to a larger vorticity-induced velocity at the bubble tip (u_b^{ω}) than at the spike tip (u_s^{ω}). In the following, the bulk velocities (u_b^{bulk} and u_s^{bulk}) and the vorticity-induced velocities (u_b^{ω} and u_s^{ω}) are first quantified theoretically, and their combined contributions to finger growth are then evaluated.

(i) Bulk velocities. For a 2-D single-mode interface entirely situated within the rarefaction region, the bulk velocity (u^{bulk}) and displacement (x^{bulk}) of any point on the interface can be described by the following 1-D characteristic relations (Gao *et al.* 2024)

$$u^{bulk}(t) = \zeta_1 t^{\theta_1} + \zeta_2 t^{\theta_2} - \frac{2}{\gamma_R - 1} c_{R0}, \tag{3.1}$$

$$x^{bulk}(t) = \frac{\zeta_1}{\theta_1 + 1} t^{\theta_1 + 1} + \frac{\zeta_2}{\theta_2 + 1} t^{\theta_2 + 1} - \frac{2}{\gamma_R - 1} c_{R0} t + \kappa, \tag{3.2}$$

https://doi.org/10.1017/jfm.2026.11898 Published online by Cambridge University Press

with

$$\theta_{1,2} = \left(-1 \pm \sqrt{1 - \frac{4p_{R0}}{\rho_{R0}} \frac{2\gamma_R(\gamma_R - 1)}{(\gamma_R + 1)^2 c_{R0}^2}} \right) /2. \tag{3.3}$$

Here, γ_R, p_{R0}, ρ_{R0} and c_{R0} denote, respectively, the adiabatic index, initial pressure, density and sound speed of the fluid on the right side of the interface. The signs '$\pm$' correspond to θ_1 and θ_2, respectively. The coefficients $\zeta_{1,2}$ and κ are undetermined parameters that depend on the initial location of the interface's target point relative to the diaphragm. Note that, although (3.1) and (3.2) appear explicitly time-dependent, their spatial dependence is implicit, arising from the interface's motion in the rarefaction-driven flow.

To determine $\zeta_{1,2}$ and κ for the bubble tip, five constraint equations are employed, introducing two auxiliary variables, t_n and x_n

$$u_b^{bulk}(t_{L0}) = 0, \tag{3.4a}$$

$$x_b^{bulk}(t_{L0}) = x_{L0}, \tag{3.4b}$$

$$u_b^{bulk}(t_n) = u_n, \tag{3.4c}$$

$$x_b^{bulk}(t_n) = x_n, \tag{3.4d}$$

$$\frac{x_n}{t_n} = c_{L0} + \frac{\gamma_L + 1}{2} u_p, \tag{3.4e}$$

where x_b^{bulk} denotes the bulk displacement at the bubble tip. (3.4*a*) and (3.4*b*) specify the initial conditions when the incident wavefront just reaches the bubble tip, located at x_{L0}. (3.4*c*) and (3.4*d*) represent the terminal conditions, where t_n and x_n denote the time and location at which the rarefaction tail encounters the bubble tip, and u_n represents the flow velocity in the region formed between the transmitted and reflected rarefaction waves once the rarefaction tail has traversed the bubble tip. (3.4*e*) is given by the geometric relation of the rarefaction tail, where c_{L0} and γ_L are the initial sound speed and adiabatic index on the left side of the interface, and u_p is the flow velocity at the rarefaction tail in the absence of reflected waves. Both u_n and u_p can be determined from 1-D gas dynamics theories (Han & Yin 1993). Equations (3.4*a*)–(3.4*e*) form a closed system for ζ_1, ζ_2, κ, t_n and x_n. By substituting (3.1) and (3.2) into (3.4*a*)–(3.4*d*) and applying (3.4*e*), the values of ζ_1, ζ_2 and κ for the bubble tip can be determined numerically. The bulk velocity and displacement of the bubble tip, u_b^{bulk} and x_b^{bulk}, can then be calculated from (3.1) and (3.2), respectively.

Because the TRF reaches the spike tip earlier than the IRF, only the downstream side of the spike tip lies within the rarefaction region during the WT stage. This feature is illustrated by the streamwise velocity field in figure 5(*i*), which presents the region enclosed by the blue dotted line in figure 5(*c*). The upstream side of the spike tip remains in the pre-IRF region and thus stays at rest, whereas the downstream side lies in the post-TRF region with a non-zero velocity. As a result, (3.1) and (3.2) are not applicable to the spike-tip motion, since both equations assume that the interface is fully immersed in the rarefaction region.

During the WT stage, the velocity immediately downstream of the spike tip is denoted by Δu_t (see figure 5*i*), which represents the velocity increment relative to the pre-TRF state. Because the normal velocity is continuous across the interface, the bulk velocity, u_s^{bulk}, can be approximated as the momentum-weighted average of the velocities on the

https://doi.org/10.1017/jfm.2026.11898 Published online by Cambridge University Press

two sides of the spike tip (0 upstream and Δu_t downstream)

$$u_s^{bulk}(t) = \frac{\rho_{R0}\Delta u_t(t)}{\rho_{L0} + \rho_{R0}}, \tag{3.5}$$

where ρ_{L0} denotes the initial density on the left side of the interface.

In (3.5), $\Delta u_t(t)$ remains unknown. Under the linear acoustic approximation (Liepmann & Roshko 1957; Whitham 1974), Δu_t is related to Δu_i (which denotes the velocity increment immediately behind the IRF relative to the velocity ahead of it) as

$$\frac{\Delta u_t}{c_{R0}} = \frac{\Delta u_i}{c_{L0}} \frac{2Z_L}{Z_L + Z_R}, \tag{3.6}$$

where $Z_L = \rho_{L0}c_{L0}$ and $Z_R = \rho_{R0}c_{R0}$ denote the acoustic impedances of the gases on the left and right sides of the interface, respectively, and the quantity Δu_i is given by

$$\Delta u_i(t) = -\frac{2c_{L0}}{\gamma_L + 1} \frac{t - t_{L0}}{t}, \ t_{L0} \leqslant t \leqslant t_{R0}. \tag{3.7}$$

Using (3.6), Δu_t can be obtained, and the bulk velocity u_s^{bulk} is then determined from (3.5).

(ii) Vorticity-induced velocities. As shown in figure 5(*e–f*), as the IRF progressively sweeps across the interface, vorticity is generated and deposited along the interface from upstream to downstream, with a higher concentration near the bubble region. This vorticity deposition, resulting from the misalignment of the density ($\nabla\rho$) and pressure (∇p) gradients, is governed by the 2-D vorticity equation

$$\frac{\mathrm{d}\omega}{\mathrm{d}t} = \frac{1}{\rho^2}\nabla\rho \times \nabla p, \tag{3.8}$$

where the expressions of $\nabla\rho$ and ∇p need to be determined.

To construct $\nabla\rho$ and ∇p, the spatio-temporally varying density and pressure fields in the rarefaction region are first established. Since the rarefaction-wave field remains isentropic (Han & Yin 1993), the density and pressure fields satisfy the following relations:

$$\rho_R(x, y, t) = \rho_{R0}C_{\rho R}(x, y, t), \quad \rho_L(x, y, t) = \rho_{L0}C_{\rho L}(x, y, t), \tag{3.9a}$$

$$p_R(x, y, t) = p_{R0}C_{pR}(x, y, t), \quad p_L(x, y, t) = p_{L0}C_{pL}(x, y, t). \tag{3.9b}$$

Here, p_R and p_L denote the instantaneous pressures on the right and left sides of the interface, and p_{L0} is the corresponding initial value on the left side. The parameters $C_{\rho R}$, $C_{\rho L}$, C_{pR} and C_{pL} represent dimensionless evolution functions that describe the spatial-temporal variations of density and pressure in the downstream and upstream regions (see Appendix B for their detailed derivations). The density and pressure at any location and time within the entire flow field can thus be constructed as follows:

$$\rho = (\rho_{R0}C_{\rho R} - \rho_{L0}C_{\rho L})H(\phi_1(x, t)) + \rho_{L0}C_{\rho L}, \tag{3.10a}$$

$$p = (p_{R0}C_{pR} - p_{L0}C_{pL})H(\phi_1(x, t)) + p_{L0}C_{pL}, \tag{3.10b}$$

where $\phi_1(x, t)$ indicates the position of the interface at time t, defined as

$$\phi_1(x, t) = x - [\eta(t)\cos(ky) + x_e(t)]. \tag{3.11}$$

https://doi.org/10.1017/jfm.2026.11898 Published online by Cambridge University Press

Here, $k = 2\pi/\lambda$ is the wavenumber, $\eta(t)$ and $x_e(t)$ denote the amplitude and equilibrium position of the interface, respectively, and $H(\phi_1)$ is the generalised Heaviside function (Abarzhi *et al.* 2003*b*; Abarzhi *et al.* 2015). To represent the discontinuous variation across the interface, it may be heuristically written as

$$H(\phi_1) = \begin{cases} 0, & \phi_1 < 0, \\ \dfrac{1}{2}, & \phi_1 = 0, \\ 1, & \phi_1 > 0. \end{cases} \tag{3.12}$$

By taking the gradients of (3.10*a*) and (3.10*b*), the density and pressure gradients can be expressed as

$$\begin{aligned} \nabla\rho = &\left[\left(\rho_{R0}C_{\rho R} - \rho_{L0}C_{\rho L}\right)\delta(\phi_1)\frac{\partial\phi_1}{\partial x} + \left(\rho_{R0}\frac{\partial C_{\rho R}}{\partial x} - \rho_{L0}\frac{\partial C_{\rho L}}{\partial x}\right)H(\phi_1) + \rho_{L0}\frac{\partial C_{\rho L}}{\partial x}\right]\boldsymbol{i} \\ &+ \left[\left(\rho_{R0}C_{\rho R} - \rho_{L0}C_{\rho L}\right)\delta(\phi_1)\frac{\partial\phi_1}{\partial y} + \left(\rho_{R0}\frac{\partial C_{\rho R}}{\partial y} - \rho_{L0}\frac{\partial C_{\rho L}}{\partial y}\right)H(\phi_1) + \rho_{L0}\frac{\partial C_{\rho L}}{\partial y}\right]\boldsymbol{j}, \end{aligned} \tag{3.13}$$

and

$$\begin{aligned} \nabla p = &\left[\left(p_{R0}C_{pR} - p_{L0}C_{pL}\right)\delta(\phi_1)\frac{\partial\phi_1}{\partial x} + \left(p_{R0}\frac{\partial C_{pR}}{\partial x} - p_{L0}\frac{\partial C_{pL}}{\partial x}\right)H(\phi_1) + p_{L0}\frac{\partial C_{pL}}{\partial x}\right]\boldsymbol{i} \\ &+ \left[\left(p_{R0}C_{pR} - p_{L0}C_{pL}\right)\delta(\phi_1)\frac{\partial\phi_1}{\partial y} + \left(p_{R0}\frac{\partial C_{pR}}{\partial y} - p_{L0}\frac{\partial C_{pL}}{\partial y}\right)H(\phi_1) + p_{L0}\frac{\partial C_{pL}}{\partial y}\right]\boldsymbol{j}. \end{aligned} \tag{3.14}$$

Here the generalised Dirac delta function $\delta(\phi_1)$ (Abarzhi *et al.* 2003*b*; Abarzhi *et al.* 2015) is interpreted in the distributional sense as the derivative of the Heaviside function, $\mathrm{d}H/\mathrm{d}\phi_1$, which is defined through the following distributional property:

$$\int_{-\infty}^{\infty} f(\phi_1)\delta(\phi_1)\mathrm{d}\phi_1 = f(0). \tag{3.15}$$

Since the terms associated with $\delta(\phi_1)$ are localised at the interface ($\phi_1 = 0$), they dominate the local interfacial gradient field. The density gradient at the interface can thus be approximated as

$$\nabla\rho = \left[\left(\rho_{R0}C_{\rho R} - \rho_{L0}C_{\rho L}\right)\delta(\phi_1)\frac{\partial\phi_1}{\partial x}\right]\boldsymbol{i} + \left[\left(\rho_{R0}C_{\rho R} - \rho_{L0}C_{\rho L}\right)\delta(\phi_1)\frac{\partial\phi_1}{\partial y}\right]\boldsymbol{j}, \quad \phi_1 = 0. \tag{3.16}$$

Furthermore, owing to the pressure continuity across the interface (i.e. $p_{R0}C_{pR} = p_{L0}C_{pL}$ at $\phi_1 = 0$) and the negligible pressure variation in the y-direction (as the rarefaction wave propagates along the x-direction and the lateral coupling in the flow is weak during the short WT stage), the pressure gradient at the interface simplifies to

$$\nabla p = \frac{1}{2}\left(p_{R0}\frac{\partial C_{pR}}{\partial x} + p_{L0}\frac{\partial C_{pL}}{\partial x}\right)\boldsymbol{i}, \quad \phi_1 = 0. \tag{3.17}$$

https://doi.org/10.1017/jfm.2026.11898 Published online by Cambridge University Press

Substituting (3.16) and (3.17) into (3.8), the vorticity generation rate at the interface can be expressed as

$$\frac{\mathrm{d}\omega}{\mathrm{d}t} = -\frac{2}{(\rho_{R0}+\rho_{L0})^2}\left(p_{R0}\frac{\partial C_{pR}}{\partial x}+p_{L0}\frac{\partial C_{pL}}{\partial x}\right)\left(\rho_{R0}C_{\rho R}-\rho_{L0}C_{\rho L}\right)\delta(\phi_1)\frac{\partial \phi_1}{\partial y},\quad \phi_1=0. \tag{3.18}$$

At any point on the interface, the velocity induced by the vortex sheet can be obtained using the Birkhoff–Rott equation, which relates the induced velocity to the distribution of vortex sheet strength along the interface

$$\boldsymbol{v}=\frac{1}{2\pi}\int_0^{\lambda}\frac{\mathrm{d}\Gamma}{\mathrm{d}l}(l')\frac{}{\boldsymbol{r}-\boldsymbol{r'}}\mathrm{d}l', \tag{3.19}$$

where $\mathrm{d}\Gamma/\mathrm{d}l$ denotes the vortex sheet strength per unit length, and $\boldsymbol{r}-\boldsymbol{r'}$ is the displacement vector from a source point to the target point. The velocity $\boldsymbol{v}_{tp}$ induced at a target point (x_0, y_0) on the interface by the vortex sheet element located at (x, y) is given by

$$\boldsymbol{v}_{tp}=\frac{1}{2\pi}\frac{(y-y_0,\, x_0-\eta(t)\cos(ky))}{(x_0-\eta(t)\cos(ky)-x_e(t))^2+(y-y_0)^2}\frac{\mathrm{d}\Gamma}{\mathrm{d}y}(y,t). \tag{3.20}$$

The x-component of this velocity can be written as

$$u^{\omega}=\frac{1}{2\pi}\frac{y-y_0}{(x_0-\eta(t)\cos(ky)-x_e(t))^2+(y-y_0)^2}\frac{\mathrm{d}\Gamma}{\mathrm{d}y}(y,t). \tag{3.21}$$

Based on (3.18), the vortex sheet strength along the interface is obtained by integrating the vorticity over the streamwise domain $x\in[-\eta(t)+x_e(t),\,\eta(t)+x_e(t)]$

$$\begin{aligned}\frac{\mathrm{d}\Gamma}{\mathrm{d}y}&=\int\omega\mathrm{d}x\\&=\int\int-\frac{2}{(\rho_{R0}+\rho_{L0})^2}\left(p_{R0}\frac{\partial C_{pR}}{\partial x}+p_{L0}\frac{\partial C_{pL}}{\partial x}\right)\left(\rho_{R0}C_{\rho R}-\rho_{L0}C_{\rho L}\right)\delta(\phi_1)\frac{\partial\phi_1}{\partial y}\mathrm{d}x\mathrm{d}t.\end{aligned} \tag{3.22}$$

Since (3.22) contains the Dirac delta function, it cannot be evaluated through conventional integration. By invoking the normalisation property of the delta function

$$\int_{-\infty}^{\infty}\delta(x)\mathrm{d}x=1, \tag{3.23}$$

which follows directly from (3.15) by setting $f(\phi_1)=1$, the Dirac delta function in (3.22) can be integrated out. Equation (3.22) is thereby simplified to

$$\frac{\mathrm{d}\Gamma}{\mathrm{d}y}=\int-\frac{2}{(\rho_{R0}+\rho_{L0})^2}\left(p_{R0}\frac{\partial C_{pR}}{\partial x}+p_{L0}\frac{\partial C_{pL}}{\partial x}\right)\left(\rho_{R0}C_{\rho R}-\rho_{L0}C_{\rho L}\right)\frac{\partial\phi_1}{\partial y}\mathrm{d}t\big|_{\phi_1=0}. \tag{3.24}$$

Finally, substituting (3.24) and the coordinates of the interface peak $(\eta(t)+x_e(t),\,0)$ and trough $(-\eta(t)+x_e(t),\,\lambda/2)$ into (3.21), and summing the contributions from all interface points, yields the total vorticity-induced velocity components in the x-direction at the bubble (u_b^{ω}) and spike tips (u_s^{ω}). In the formulation of the vorticity-induced

https://doi.org/10.1017/jfm.2026.11898 Published online by Cambridge University Press

velocities, the spatio-temporal characteristics of the rarefaction-driven flow are inherently incorporated through the coefficients $C_{\rho R}$, C_{pR}, $C_{\rho L}$ and C_{pL}, which depend on both time t and spatial coordinate x (see (B8a), (B8b), (B15a) and (B15b) in Appendix B).

Notably, because the rarefaction field is compressible, the propagation of vorticity-induced velocity information to the finger tip requires a finite time. This propagation is assumed to follow the principle of minimum travel time, and the propagation speed is taken as the initial sound speed of the light fluid, c_{R0}, which represents the maximum characteristic speed in the system. The propagation path is assumed to follow the interface, leading to a finite delay time (Δt^{ω}) for the velocity information

$$\Delta t^{\omega} = \frac{\left| \int_{y}^{y_0} \sqrt{1+\eta(t)^2 k^2 \sin^2(ky)}\,\mathrm{d}y \right|}{c_{R0}}. \tag{3.25}$$

In practical calculations, the vorticity-induced velocity computed at a given time step is therefore applied to the finger growth with a delay of Δt^{ω}, accounting for its finite propagation time along the interface.

(iii) Total velocity. Based on the Helmholtz decomposition of velocity, the instantaneous velocities of the bubble tip (u_b) and spike tip (u_s) during the WT stage can be expressed as the sum of the bulk and vorticity-induced components

$$u_b(t) = u_b^{bulk}(t) + u_b^{\omega}(t), \tag{3.26a}$$

$$u_s(t) = u_s^{bulk}(t) + u_s^{\omega}(t). \tag{3.26b}$$

The corresponding tip positions, $x_b(t)$ and $x_s(t)$, are obtained by temporal integration of the respective velocities. The bubble and spike growth rates, $V_{b/s}^{theo}$, and amplitudes, $\eta_{b/s}^{theo}$, are defined relative to a flat interface, whose instantaneous velocity u_f and position x_f are given by (3.1) and (3.2), respectively,

$$V_b^{theo}(t) = u_b(t) - u_f(t), \quad V_s^{theo}(t) = u_f(t) - u_s(t), \tag{3.27a}$$

$$\eta_b^{theo}(t) = x_b(t) - x_f(t), \quad \eta_s^{theo}(t) = x_f(t) - x_s(t). \tag{3.27b}$$

Table 3 summarises the theoretical finger amplitudes and growth rates at the end of the WT stage, together with the results from numerical simulations for comparison. As the initial amplitude increases, both bubble and spike amplitudes as well as their velocities grow progressively by the end of the WT stage. For $\eta_0/\lambda \geqslant 0.2$, the bubble (spike) growth rate exceeds 5.0 (2.5) m s^{-1}, and for $\eta_0/\lambda = 0.5$, it reaches approximately 16.5 (6.0) m s^{-1}. These results indicate that under high-amplitude conditions, finger growth during the WT stage becomes pronounced, and its influence on subsequent linear and nonlinear evolution cannot be neglected. The bubble consistently exhibits a higher growth rate than the spike, as its upstream position exposes it to stronger rarefaction effects, resulting in greater contributions from both bulk motion and baroclinic vorticity. Overall, the theoretical predictions of bubble/spike amplitudes and growth rates at the end of the WT stage agree with the numerical results.

To characterise the relative importance of the bulk and vorticity contributions on finger growth, we define two proportional factors

$$\Lambda_b = [u_b^{bulk}(t) - u_f(t)]/u_b^{\omega}(t), \tag{3.28a}$$

$$\Lambda_s = [u_f(t) - u_s^{bulk}(t)]/u_s^{\omega}(t). \tag{3.28b}$$

https://doi.org/10.1017/jfm.2026.11898 Published online by Cambridge University Press

Cases	Δt_{WT}	η_b^{theo}	η_b^{num}	η_s^{theo}	η_s^{num}	V_b^{theo}	V_b^{num}	V_s^{theo}	V_s^{num}
2-40	21.5	2.01	2.01	2.00	2.01	0.76	0.68	0.54	0.51
4-40	42.9	4.05	4.06	4.03	4.05	1.92	1.98	1.33	1.59
8-40	85.9	8.25	8.25	8.05	8.11	5.00	5.02	2.55	2.91
12-40	128.8	12.64	12.67	12.10	12.19	8.68	8.70	3.82	4.00
16-40	171.7	17.21	17.31	16.16	16.27	12.53	13.38	5.01	5.02
20-40	214.6	21.99	22.10	20.23	20.39	16.52	17.03	6.07	6.00

Table 3. Comparison of theoretical and numerical results for finger amplitudes and growth rates at the end of the WT stage. Here, Δt_{WT} is the duration of the WT stage, $\eta_{b/s}^{theo}$ ($\eta_{b/s}^{num}$) are the theoretical (numerical) bubble/spike amplitudes and $V_{b/s}^{theo}$ ($V_{b/s}^{num}$) are the corresponding growth rates. Time, length and velocity are given in μs, mm and m s^{-1}, respectively.

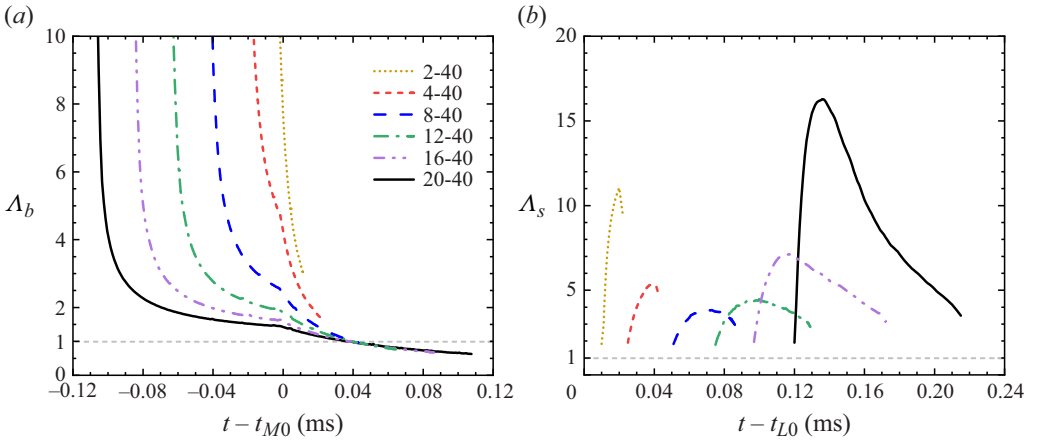


Figure 6. Temporal evolution for proportional factors Λ_b (a) and Λ_s (b).

Figures 6(a) and 6(b) show the temporal evolutions of Λ_b and Λ_s, respectively. For clarity, the time axes in panels (a,b) are shifted by subtracting t_{M0} and t_{L0}, with t_{M0} denoting the moment when the IRF reaches the interface's initial equilibrium position. For bubbles, the rarefaction wave initially induces a bulk velocity that greatly exceeds the vorticity-induced velocity due to minimal vorticity deposition. As the amount of deposited vorticity grows, Λ_b rapidly drops to approximately 2.5 before exhibiting a slower decay. This slower decay occurs because the deposited vorticity is progressively farther away from the bubble tip, weakening its contribution. For cases 2-40 and 4-40, the deposited vorticity remains limited and Λ_b stays above unity, implying that the bulk contribution dominates throughout the WT stage. In contrast, for cases 8-40, 12-40, 16-40 and 20-40, Λ_b drops below unity at late times, indicating that vorticity effects eventually govern the bubble dynamics. Notably, the Λ_b curve exhibits a slight inflection at $t = t_{M0}$, reflecting the onset of motion at the equilibrium position triggered by the rarefaction wave.

For spikes, Λ_s exhibits a rise–peak–decay trend for all cases during the WT stage. Throughout this stage, the spike dynamics is governed by the bulk effect ($\Lambda_s > 1$), since most vorticity is generated near the bubble region and its influence on the spike motion remains limited. The peak value of Λ_s varies non-monotonically with η_0/λ: it first decreases because stronger vorticity deposition at higher η_0/λ enhances the vorticity

https://doi.org/10.1017/jfm.2026.11898 Published online by Cambridge University Press

contribution, but rises again at even higher η_0/λ as the greater initial amplitude displaces the dominant vorticity region farther from the spike tip, thereby weakening its influence on spike growth.

3.3.2. *Linear and nonlinear stages*

After the WT stage, the entire interface is fully immersed in the rarefaction field, and the perturbation growth subsequently enters the linear and nonlinear stages. Figure 7(a–f) presents the experimental amplitude evolution under different η_0/λ conditions. For comparison, the low-amplitude case 2-40 from previous experiments (Li *et al.* 2025) is included in figure 7(a). The evolving interface amplitude (η) is defined as half the distance between the bubble and spike tips. When secondary instabilities develop at the finger tips, the bubble (or spike) tip position is taken as the average location of the small perturbations in the flow direction, and the associated error bars denote the spatial extent of these perturbations in that direction. In high-amplitude cases (figure 7b–f), after the WT stage, perturbation growth rapidly departs from the linear regime and transitions into the quasi-steady stage with an approximately constant growth rate. A subsequent reduction in growth rate, as shown in the light blue region of figure 7(c–f), is mainly attributed to bubble deceleration, which will be discussed in § 3.4.

Recently, Li *et al.* (2025) extended Layzer's potential-flow framework to incorporate time-dependent acceleration and density, allowing the description of rarefaction-driven finger growth up to the quasi-steady phase. This model has been shown to accurately predict the evolution of low-amplitude RTI; however, its applicability to high-amplitude cases remains unverified. The bubble and spike growth rates, V, which share a unified formulation across the linear, weakly nonlinear and quasi-steady stages, are obtained by solving the following equation:

$$\frac{\mathrm{d}V}{\mathrm{d}t} = -\frac{S_2 v^2 + S_3}{S_1}, \tag{3.29}$$

where

$$S_1 = F_1 + F_2 \frac{\mathrm{d}\xi}{\mathrm{d}\eta}, \tag{3.30a}$$

$$S_2 = F_2 \frac{d^2\xi}{\mathrm{d}\eta^2} + F_3 \left[k^2 c^2 + 16 \left(\frac{\mathrm{d}\xi}{\mathrm{d}\eta} \right)^2 \right] + F_4(-6-\alpha) \left(\frac{\mathrm{d}\xi}{\mathrm{d}\eta} \right)^2, \tag{3.30b}$$

$$S_3 = [F_5 + F_6(-6-\alpha)] \frac{\mathrm{d}\xi}{\mathrm{d}\eta} V + F_7. \tag{3.30c}$$

Here, the finger curvature ξ, correlated with the finger amplitude η, is expressed as

$$\xi(\eta) = -\frac{3+A}{12\sqrt{2(1+A)}} + \left[-\frac{k\eta_0}{2} + \frac{3+A}{12\sqrt{2(1+A)}} \right] e^{-3k(\eta-\eta_0)}. \tag{3.31}$$

The function $c(t)$ in (3.30b), introduced to ensure the convergence of spike growth, can be expressed as

$$c(t) = (-6+\alpha)\xi(t), \tag{3.32}$$

with

$$\alpha = \frac{-\dot{\rho}_2 \rho_1}{\dot{\rho}_1 \rho_2 + \dot{\rho}_2 \rho_1}. \tag{3.33}$$

https://doi.org/10.1017/jfm.2026.11898 Published online by Cambridge University Press

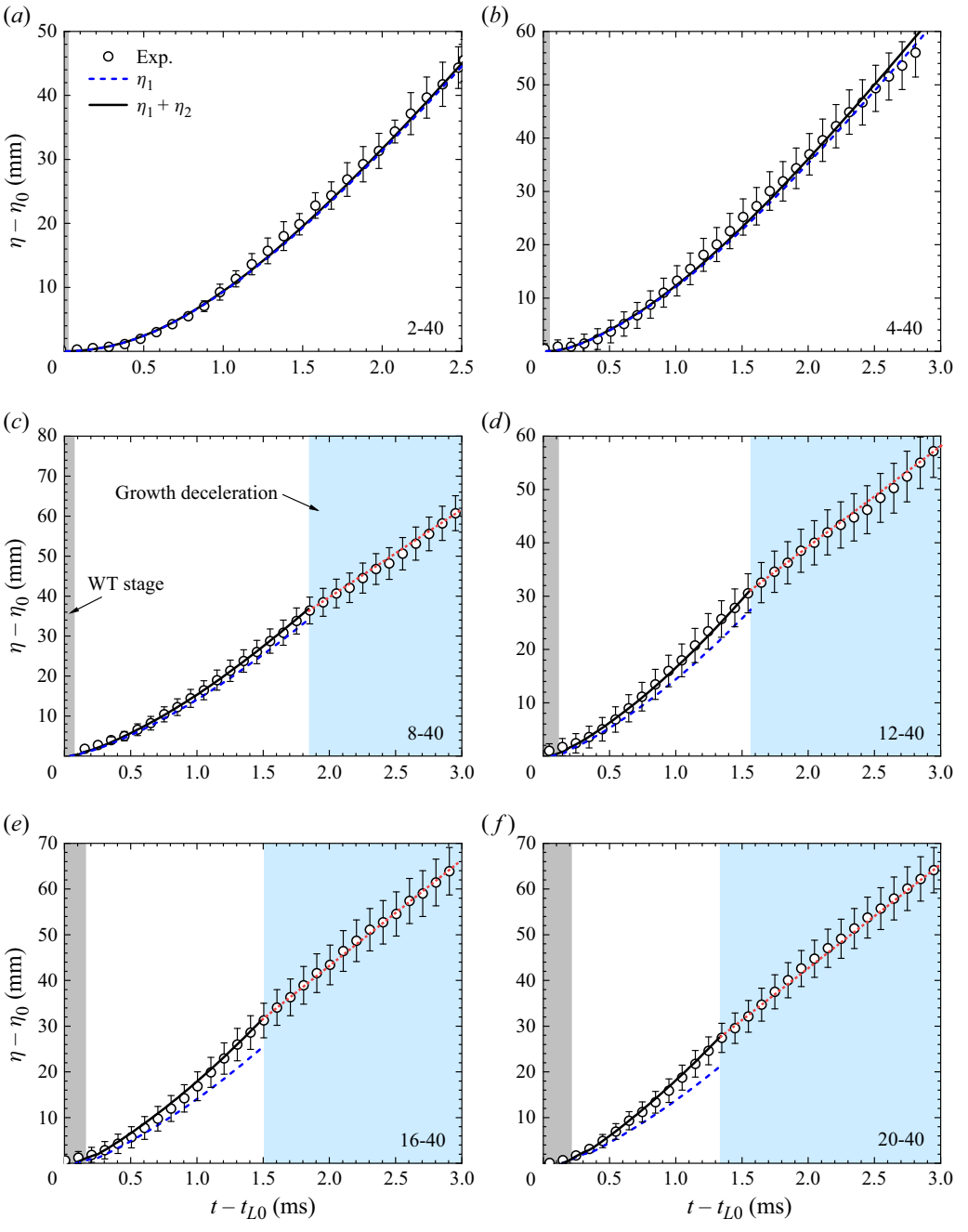


Figure 7. Comparisons of finger growth between the experimental measurements and theoretical predictions. Panel (*a*) shows the data of the low-amplitude case 2-40 from previous experiments (Li *et al.* 2025). Here, η_1 denotes the RTI-induced amplitude obtained from (3.29), while η_2 corresponds to the amplitude resulting from interface stretching. The red dotted line, serving as an auxiliary reference, indicates the perturbation growth deceleration.

https://doi.org/10.1017/jfm.2026.11898 Published online by Cambridge University Press

In the unified formulation of Li *et al.* (2025), ρ_1 and ρ_2 denote the densities of the two fluids, with overdots indicating time derivatives. For bubbles, ρ_1 and ρ_2 correspond to the heavy and light fluids, resulting in $A > 0$; for spikes, ρ_1 and ρ_2 correspond to the light and heavy fluids, resulting in $A < 0$. According to (3.9*a*), the time-dependent densities for the light and heavy fluids, $\rho_l(t)$ and $\rho_h(t)$, can be written as

$$\rho_l(t) = \rho_R(t) = \rho_{R0} C_{\rho R}, \tag{3.34a}$$

$$\rho_h(t) = \rho_L(t) = \rho_{L0} C_{\rho L}, \tag{3.34b}$$

where $C_{\rho R}$ and $C_{\rho L}$ are given by (B8*a*) and (B15*a*) in Appendix B, respectively. The coefficients F_1–F_7 are expressed as

$$F_1 = 2k\xi(-\rho_1 + \rho_2) - \frac{kc\rho_1}{1 + c + 6\xi} - \frac{kc\rho_2}{1 + c - 6\xi}, \tag{3.35a}$$

$$F_2 = \frac{2\rho_1}{1 + c + 6\xi} + \frac{2\rho_2}{1 + c - 6\xi}, \tag{3.35b}$$

$$F_3 = \frac{-\rho_1}{(1 + c + 6\xi)^2} + \frac{\rho_2}{(1 + c - 6\xi)^2}, \tag{3.35c}$$

$$F_4 = \frac{-2\rho_1}{(1 + c + 6\xi)^2} + \frac{-2\rho_2}{(1 + c - 6\xi)^2}, \tag{3.35d}$$

$$F_5 = \frac{10kc\dot{\eta}\rho_1 + 2(1 + c - 4\xi + 5kc\eta)\dot{\rho}_1}{(1 + c + 6\xi)^2} + \frac{-10kc\dot{\eta}\rho_2 + 2(1 + c + 4\xi - 5kc\eta)\dot{\rho}_2}{(1 + c - 6\xi)^2}, \tag{3.35e}$$

$$F_6 = \frac{(-1 - 6\xi)k\dot{\eta}\rho_1 - (2\xi + k\eta + 6k\eta\xi)\dot{\rho}_1}{(1 + c + 6\xi)^2} + \frac{(-1 + 6\xi)k\dot{\eta}\rho_2 - (2\xi + k\eta - 6k\eta\xi)\dot{\rho}_2}{(1 + c - 6\xi)^2}, \tag{3.35f}$$

$$\begin{aligned} F_7 = &-\frac{kc\dot{\eta}\dot{\rho}_1(2kc\eta + c + 2\xi + 1)}{(1 + c + 6\xi)^2} - \frac{\dot{\rho}_1^2(kc\eta - 2\xi)(kc\eta - c - 8\xi - 1)}{\rho_1(1 + c + 6\xi)^2} - 2kg\rho_1\xi \\ &+ \frac{kc\dot{\eta}\dot{\rho}_2(2kc\eta - c + 2\xi - 1)}{(1 + c - 6\xi)^2} + \frac{\dot{\rho}_2^2(kc\eta - 2\xi)(kc\eta + c - 8\xi + 1)}{\rho_2(1 + c - 6\xi)^2} + 2kg\rho_2\xi \\ &+ \frac{\ddot{\rho}_1(2\xi - kc\eta)}{1 + c + 6\xi} + \frac{\ddot{\rho}_2(2\xi - kc\eta)}{1 + c - 6\xi}, \end{aligned} \tag{3.35g}$$

where g is the rarefaction-induced interface acceleration and can be obtained by the time derivative of (3.1)

$$g(t) = \theta_1\zeta_1 t^{\theta_1 - 1} + \theta_2\zeta_2 t^{\theta_2 - 1}. \tag{3.36}$$

Note that the spatial dependence is implicitly incorporated in (3.36), since it describes the acceleration experienced by an interface that continuously moves within the rarefaction-driven flow field. Within the unified formulation (3.29), the bubble solution is obtained by taking $A > 0$ and $g > 0$, whereas the spike solution corresponds to $A < 0$ and $g < 0$. The model (3.29) reduces to the variable-acceleration form when the density-derivative term is neglected and further simplifies to the constant-acceleration, constant-density limit when both density and acceleration variations vanish. Further details about the model can be

https://doi.org/10.1017/jfm.2026.11898 Published online by Cambridge University Press

found in Li *et al.* (2025). For high-amplitude cases, the contribution of the WT stage becomes significant and is incorporated into the model by using the finger amplitude and velocity at the end of the WT stage as initial conditions for (3.29). The RTI interface amplitude, defined as η_1, is then obtained by computing the bubble and spike amplitudes from (3.29) and taking their average.

During the linear and nonlinear stages, both bubble and spike tips are completely immersed in the rarefaction region, and the bulk velocity difference between the tips may lead to significant interface stretching. To quantify this effect, the bulk displacements of the bubble and spike tips are first described by (3.2). Similar to the procedure for the bubble case, by taking the spike-tip velocity $u_s^{bulk}(t_{R0})$ and position x_{R0} at the end of the WT stage as the initial conditions and substituting them into (3.4*a*) and (3.4*b*), new values of $\zeta_{1,2}$ and κ can be obtained to characterise the spike-tip position. The corresponding stretching-induced amplitudes for bubbles and spikes, η_b^s and η_s^s, are then obtained from

$$\eta_b^s(t) = \int [u_b^{bulk}(t) - u_f(t)]\,\mathrm{d}t, \tag{3.37a}$$

$$\eta_s^s(t) = \int [u_f(t) - u_s^{bulk}(t)]\,\mathrm{d}t. \tag{3.37b}$$

The average of these two amplitudes defines the stretching-induced interface amplitude, denoted by η_2.

Figure 7(*a*–*f*) compares the experimental amplitude evolution with the theoretical predictions of η_1 and $\eta_1 + \eta_2$. Since the model does not account for deceleration in perturbation growth, the comparison is valid only prior to its onset. For cases 2-40 and 4-40, where the stretching effect is weak, the η_1 and $\eta_1 + \eta_2$ predictions are close and both agree well with the experimental results. In contrast, for cases 8-40, 12-40, 16-40 and 20-40, the η_1 curve falls below the experimental amplitudes as interface stretching becomes increasingly pronounced, whereas the $\eta_1 + \eta_2$ prediction effectively captures the growth up to the onset of deceleration. The success of the linear superposition of η_1 and η_2 in reproducing the measured amplitudes suggests that, within the present parameter range, the rarefaction-induced background flow and the instability-induced dynamics can be approximately treated as separable.

As illustrated by Mikaelian (2008), Layzer-type potential-flow models can break down under high-amplitude conditions, and model (3.29) is no exception. Specifically, when η_0/λ exceeds a certain threshold, the denominator (S_1) of model (3.29) vanishes as the interface curvature evolves, rendering the model mathematically ill posed. Recently, Liu *et al.* (2023*a*,*b*) isolated the effect of curvature on RTI evolution within the Layzer potential framework, demonstrating that curvature effects strengthen with increasing η_0/λ and result in an overshoot in the bubble growth rate. However, at high amplitudes, the singularity issue inherent to Layzer-type models remains unresolved. Zhang & Guo (2016) proposed prescribing the finger curvature as its quasi-steady value from the onset of the evolution, thereby avoiding the singularity caused by curvature evolution. Nevertheless, recent studies (Li *et al.* 2025) have shown that this treatment is valid only for moderate values of η_0/λ; for both very low and very large values of η_0/λ, the initial and quasi-steady curvatures differ significantly, making the treatment inappropriate. For rarefaction-driven RTI in the present work, the finger curvature evolves rapidly under high η_0/λ, and the critical curvature corresponding to $S_1 = 0$ is reached within the WT stage. As a result, the singularity can be avoided by initialising (3.29) with the amplitude and velocity at the end of the WT stage. It is worth noting that RTI driven by accelerations which are applied instantaneously to the entire interface (e.g. gravity- or mechanically driven RTI)

https://doi.org/10.1017/jfm.2026.11898 Published online by Cambridge University Press

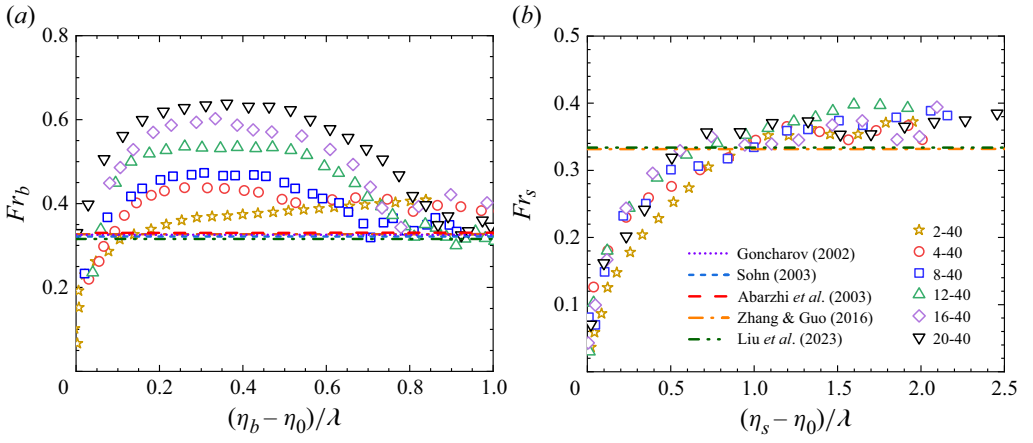


Figure 8. Evolution of bubble (a) and spike (b) Froude numbers under different η_0/λ. Lines indicate the predictions of potential-flow models under constant acceleration and density.

does not possess a WT stage. Nevertheless, when modelling such high-amplitude RTI, an artificial 'WT-like' stage, or equivalently a vorticity-deposition stage, can be introduced in the early regime to allow sufficient curvature development and thereby prevent the singularity. During this stage, perturbation growth may be described using a vortex-based model (Jacobs & Sheeley 1996), which generally performs well at early times; thereafter, the conventional potential-flow formulation can be employed to capture the subsequent evolution.

3.4. *Finger dynamics*

3.4.1. *Froude-number evolution*

The Froude number is often used to scale the bubble and spike growth rates to evaluate the finger dynamics. According to Ramaprabhu *et al.* (2006), the Froude numbers for bubbles (Fr_b) and spikes (Fr_s) are defined as

$$Fr_{b/s} = \frac{V_{b/s}}{\sqrt{Ag\lambda/(1 \pm A)}}, \tag{3.38}$$

where $V_{b/s}$ denotes the bubble and spike growth rates, respectively; and the signs '$\pm$' correspond to bubbles and spikes, respectively. Under constant acceleration and density, several potential-flow models have been developed to predict the quasi-steady growth rates of bubbles (V_b^{qs}) and spikes (V_s^{qs}) (Goncharov 2002; Abarzhi *et al.* 2003*a*; Sohn 2003; Zhang & Guo 2016; Liu *et al.* 2023*b*). Substituting the expressions of V_b^{qs} and V_s^{qs} into (3.38) yields the corresponding quasi-steady Froude numbers for bubbles and spikes, respectively. The expressions of V_b^{qs} and V_s^{qs} from these potential-flow models, together with the resulting Froude numbers, are summarised in table 4.

Figures 8(a) and 8(b) show the temporal evolution of experimental Fr_b and Fr_s, plotted against $(\eta_{b/s} - \eta_0)/\lambda$, under different η_0/λ conditions. Theoretical predictions obtained from different potential-flow models are also included for comparison. As illustrated in table 4, the Fr_b value obtained from the model of Goncharov (2002) is constant, while the remaining Froude-number models are functions of A. Here, the time-varying values of A are substituted into these models to obtain the theoretical lines. Since A varies only slightly during the experimental time (see figure 3b), these theoretical lines are nearly horizontal,

https://doi.org/10.1017/jfm.2026.11898 Published online by Cambridge University Press

Model	$V_{b/s}^{qs}$	$Fr_{b/s}^{qs}$
Goncharov (2002)	$\sqrt{\frac{2A}{1+A}\frac{g}{3k}}$	$\sqrt{\frac{1}{3\pi}}$
Sohn (2003)	$\sqrt{\frac{Ag}{(2+A)k}}$	$\sqrt{\frac{1+A}{2\pi(2+A)}}$
Abarzhi *et al.* (2003*a*)	$\sqrt{\frac{g}{3k}}\left(1-\frac{3(1-A)}{16}\right)$	$\sqrt{\frac{1+A}{6\pi A}}\left(1-\frac{3(1-A)}{16}\right)$
Zhang & Guo (2016)	$\sqrt{\frac{8Ag}{3k(1+A)(3+A)}\frac{[3+A+\sqrt{2}(1+A)^{1/2}]^2}{4(3+A)+\sqrt{2}(9+A)(1+A)^{1/2})}}$	$\sqrt{\frac{4}{3\pi(3+A)}\frac{[3+A+\sqrt{2}(1+A)^{1/2}]^2}{4(3+A)+\sqrt{2}(9+A)(1+A)^{1/2}}}$
Liu *et al.* (2023*b*)	$(0.814-0.027A)\sqrt{\frac{Ag}{k(1+A)}}$	$(0.814-0.027A)\sqrt{\frac{1}{2\pi}}$

Table 4. Expressions of quasi-steady growth rates ($V_{b/s}^{qs}$) and Froude numbers ($Fr_{b/s}^{qs}$) for bubbles and spikes in different potential-flow models. The formulations proposed by Goncharov (2002), Sohn (2003) and Abarzhi *et al.* (2003*a*) are only valid for bubbles, while the models developed by Zhang & Guo (2016) and Liu *et al.* (2023*b*) apply to both bubbles and spikes, with $A > 0$ corresponding to bubbles and $A < 0$ to spikes.

and the predicted Froude numbers for all models are close to each other. As shown in figure 8(*a*), the experimental Fr_b for case 2-40 undergoes an initial increase followed by a quasi-steady phase. This behaviour is similar to that observed before the potential bubble re-acceleration in constant-acceleration and -density scenarios (Ramaprabhu *et al.* 2012; Wei & Livescu 2012; Bian *et al.* 2020). However, the quasi-steady value for case 2-40 exceeds that predicted by the conventional potential-flow models. This deviation is mainly attributed to the density decrease within the rarefaction field, which reduces the drag on the bubble tip. Consequently, a higher asymptotic velocity is required to balance buoyancy and drag forces, resulting in an elevated Fr_b (Guo *et al.* 2025; Li *et al.* 2025). For high-amplitude cases, Fr_b increases rapidly at early times and reaches the quasi-steady value at $(\eta_b - \eta_0)/\lambda \sim 0.2$. As η_0/λ increases, the quasi-steady value of Fr_b also increases. However, the duration of this quasi-steady stage is significantly shorter than that in low-amplitude cases. Previous low-amplitude studies have reported that the quasi-steady state of Fr_b typically persists up to at least $(\eta_b - \eta_0)/\lambda \sim 1$, and beyond this point, this quasi-steady state may terminate owing to bubble re-acceleration (Wilkinson & Jacobs 2007; Ramaprabhu *et al.* 2012; Bian *et al.* 2020). In the present work, however, the quasi-steady state under high-amplitude conditions ends $(\eta_b - \eta_0)/\lambda \sim 0.4$–$0.5$, and is terminated by bubble deceleration instead of re-acceleration. This deceleration accounts for the slowdown in amplitude growth observed in figure 7(*c*–*f*). Eventually, Fr_b for high-amplitude cases exhibits slight oscillations and approaches a saturated state. For the spike Froude number, as shown in figure 8(*b*), the Fr_s data almost collapse across different cases, indicating that the spike dynamics is largely insensitive to the initial perturbation amplitude.

3.4.2. *Mechanism interpretation of bubble behaviour*

Similar to traditional small-amplitude RTI studies (Zhou 2017*a*,*b*), the bubble evolution for case 2-40 can be divided into three stages: linear, weakly nonlinear and quasi-steady, and the first two are collectively referred to as the linear-to-weakly nonlinear (LW) stage. By contrast, high-amplitude cases exhibit two additional stages following the quasi-steady

https://doi.org/10.1017/jfm.2026.11898 Published online by Cambridge University Press

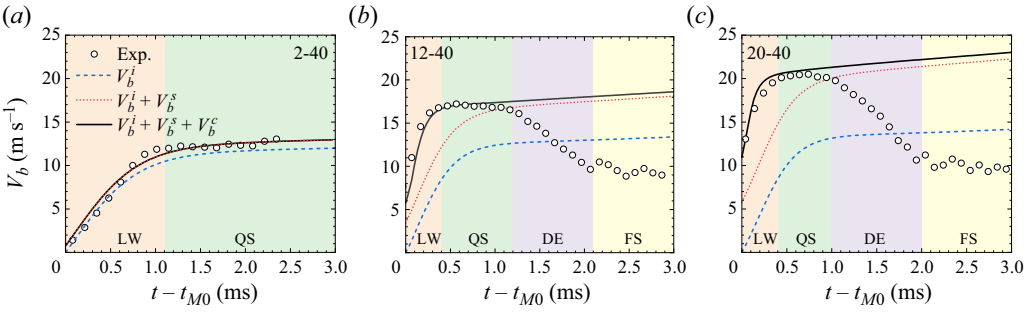


Figure 9. Comparison of the experimentally measured bubble velocity with theoretical predictions incorporating the inertial, stretching and curvature effects for cases 2-40 (*a*), 12-40 (*b*) and 20-40 (*c*). Here V_b^i, V_b^s and V_b^c denote the velocities induced by the inertial, stretching and curvature effects, respectively; LW, QS, DE and FS denote the linear-to-weakly nonlinear, quasi-steady, deceleration and fluctuating saturated stages, respectively.

stage: deceleration and fluctuating saturation. In the following, the mechanisms governing the distinct stages of bubble evolution under low- and high-amplitude conditions are elucidated.

(i) Inertial, curvature and stretching effects

For rarefaction-driven RTI, the mechanisms governing bubble growth can be classified into three contributions: (i) the inertial effect associated with the time-dependent acceleration and density field, (ii) the curvature effect arising from the bubble-front distortion and (iii) the interface-stretching effect induced by the non-uniform bulk velocities imposed by the rarefaction wave. The first two mechanisms are similar to those governing bubble evolution in constant-acceleration and constant-density flows (Liu *et al.* 2023*a*,*b*), whereas the third arises from the intrinsic characteristic of the rarefaction wave. Since the present theory provides reliable predictions of RTI perturbation growth before deceleration, it is used to quantitatively analyse bubble evolution in the LW and quasi-steady stages.

Figure 9(*a–c*) compares the experimental bubble velocity with theoretical predictions for cases 2-40, 12-40 and 20-40, respectively. In figure 9, V_b^i, V_b^s and V_b^c denote the bubble velocities induced by the inertial, stretching and curvature effects, respectively; V_b^i is obtained by directly prescribing the quasi-steady curvature ($\xi_{qs} = -(3 + A_0)/[12\sqrt{2(1 + A_0)}]$, (Zhang & Guo 2016)) in (3.29) while neglecting interface stretching throughout the evolution from the WT to nonlinear stages; $V_b^i + V_b^s$ further incorporates the stretching contribution on the basis of the inertial effect, where V_b^s is obtained as the time derivative of the stretching-induced bubble amplitude defined in (3.37*a*); $V_b^i + V_b^s + V_b^c$ represents the total contribution of the inertial, stretching and curvature effects, and its value equals the time derivative of $\eta_1 + \eta_2$. As shown in figure 9(*a*), the stretching effect is weak for case 2-40, resulting in only a slight increase in $V_b^i + V_b^s$ relative to V_b^i. Moreover, because the initial curvature ($\xi_0 = -k\eta_0/2 = -0.157$) in case 2-40 is already close to its quasi-steady value ($\xi_{qs} = -0.167$), the curvature contribution is negligible. By contrast, for cases 12-40 and 20-40, accounting for the inertial effect alone underestimates the bubble velocity during both the LW and quasi-steady stages, as shown in figures 9(*b*) and 9(*c*). When the stretching effect is included, the predicted velocity increases markedly, and $V_b^i + V_b^s$ eventually approaches the experimentally observed quasi-steady value. However, because the bubble velocity in the LW stage remains underestimated, the transition to the quasi-steady state is noticeably delayed. Once the curvature effect is incorporated,

https://doi.org/10.1017/jfm.2026.11898 Published online by Cambridge University Press

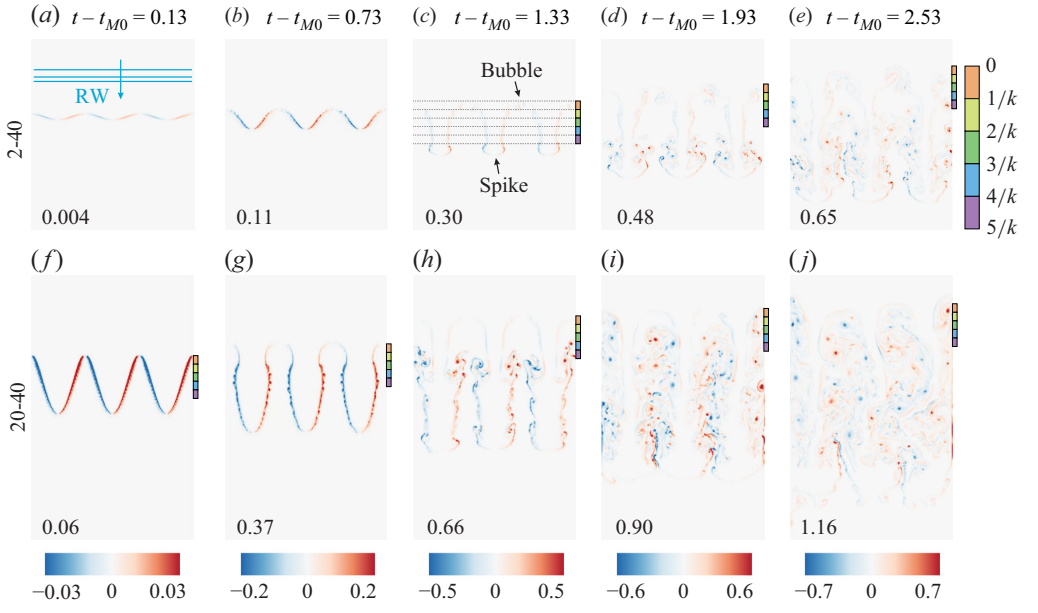


Figure 10. Visualisations of the dimensionless vorticity field, defined as $\omega^* = (\partial_x u_y - \partial_y u_x)/\sqrt{p_0/\rho_0}$, for cases 2-40 ($a$–$e$) and 20-40 ($f$–$j$). Each column corresponds to the same instant, denoted by $t - t_{M0}$ (in ms), and the number at the lower-left corner of each panel indicates $(\eta_b - \eta_0)/\lambda$.

$V_b^i + V_b^s + V_b^c$ successfully reproduces the rapid increase in bubble velocity and accurately captures the transition to the quasi-steady state, while contributing only marginally to the magnitude of the quasi-steady velocity.

Overall, in low-amplitude cases, the bubble evolution is dominated by the inertial effect, while the curvature and stretching effects are weak. In high-amplitude cases, the inertial effect provides the fundamental contribution to bubble growth, whereas the curvature effect governs the transition to the quasi-steady state and the stretching effect determines the magnitude of the quasi-steady velocity. However, the present theoretical framework is only applicable up to the quasi-steady stage and cannot accurately describe the deceleration and subsequent fluctuating saturation stages. This limitation motivates a closer examination of the underlying physical mechanism in the later stages. Notably, the inertial effect is essentially a manifestation of the action of vorticity at the bubble tip. At high amplitudes, the spike–bubble asymmetry is further enhanced, which in turn modifies the vorticity transport process (Bian *et al.* 2020). Therefore, the evolution of the vorticity field is examined in the following to further elucidate the mechanism governing bubble growth across different stages.

(ii) Vorticity dynamics

Figures 10(a–e) and 10(f–j) present the temporal evolution of the vorticity field for cases 2-40 and 20-40, respectively. The vorticity is normalised as $\omega^* = (\partial_x u_y - \partial_y u_x)/\sqrt{p_0/\rho_0}$, consistent with that used in figure 5. The time corresponding to each column is indicated at the top of the figure as $t - t_{M0}$, while the corresponding $(\eta_b - \eta_0)/\lambda$ is labelled at the lower left of each panel. To clearly illustrate the evolution of spatial distributions of the vorticity, different colour-bar ranges are adopted at different times. For case 2-40, during the early and intermediate stages (figure 10a–c, $t - t_{M0} < 1.33$ ms), the vorticity is distributed relatively uniformly along the interface. Subsequently, vortex

https://doi.org/10.1017/jfm.2026.11898 Published online by Cambridge University Press

shedding occurs from the spike (figure 10*d*). The shed vortices are then advected toward the bubble and form an approximately symmetric distribution about the vertical centreline of the spike (figure 10*e*). In contrast, for case 20-40, stronger baroclinic vorticity is deposited along the interface due to the high initial amplitude (figure 10*f*). As the interface evolves, the intense velocity shear between the light and heavy fluids on both sides of the spike arm triggers KH instability, causing vorticity to roll up into discrete vortices along the spike arms (figure 10*g*,*h*). Meanwhile, the bubble head continues to expand, where the flow is characterised by weak shear (Liu *et al.* 2023*b*), thereby suppressing local shear-induced vorticity generation. As evolution proceeds, numerous vortices begin to detach from the spike arms. These shed vortices undergo frequent interactions during their advection toward the bubble (figure 10*i*), rendering the vorticity field within the interior region increasingly disordered (figure 10*j*).

To explore which regions of vorticity have a dominant influence on the bubble dynamics, the interface is partitioned based on the vertical distance measured downward from the bubble tip. The characteristic length scale $1/k$ is used to define the partition. Accordingly, locations at 0, $1/k$, $2/k$, $\cdots$, n/k ($n = 1, 2, \cdots$) are introduced, as illustrated in figure 10(*c*). The velocity induced at the bubble tip is then evaluated using the Biot–Savart (BS) law by integrating the vorticity contained within the region extending from the tip to a vertical distance of n/k downstream. Notably, in the BS-law calculation, the stretching effect induced by the bulk velocity difference is incorporated. It is found that, using the vorticity within the region extending from the bubble tip to $5/k$, the BS-law prediction with stretching effect shows good agreement with the experimental and numerical results over the entire bubble evolution, as illustrated for cases 2-40 and 20-40 in figures 11(*a*) and 11(*d*). This indicates that the bubble dynamics is primarily governed by vorticity contained within a finite near-tip region extending up to approximately $5/k$.

To further elucidate the distinct bubble dynamics between low- and high-amplitude cases, the area-integrated vorticity is examined. The area integral of vorticity is defined as $\Gamma_{tot} = \int\int_{\Omega} \omega \mathrm{d}\Omega$, where Ω denotes the integration domain. This quantity can be decomposed into interfacial and interior contributions, denoted as $\Gamma_{interface}$ and $\Gamma_{interior}$, respectively. Figures 11(*b*) and 11(*e*) present the temporal evolution of Γ_{tot}, $\Gamma_{interface}$ and $\Gamma_{interior}$ within the 0–$5/k$ region for cases 2-40 and 20-40, respectively. For case 2-40, $\Gamma_{interface}$ increases during the early stage and remains nearly unchanged after $t \approx 1.1$ ms. In contrast, $\Gamma_{interior}$ begins to increase only after $t - t_{M0} \approx 2.0$ ms, because the shed vortices enter the 0–$5/k$ region at a relatively late stage. Although the increase in $\Gamma_{interior}$ leads to a pronounced rise in Γ_{tot}, the bubble velocity in figure 11(*a*) remains almost unaffected, suggesting that the bubble dynamics is predominantly governed by the interfacial vorticity. Overall, the nearly unchanged $\Gamma_{interface}$ after $t - t_{M0} \approx 1.1$ ms ensures sufficient interfacial vorticity to sustain bubble growth, thereby enabling the bubble velocity in case 2-40 to remain at its quasi-steady value once reached.

For case 20-40, as shown in figure 11(*e*), $\Gamma_{interface}$ begins to decrease at $t - t_{M0} \approx 1.0$ ms. Notably, the onset of bubble deceleration in figure 11(*d*) occurs at approximately the same time. This temporal correspondence suggests a direct link between the reduction of interfacial vorticity at the 0–$5/k$ region and the bubble deceleration. The value of $\Gamma_{interface}$ drops to approximately one-half of its peak value by $t - t_{M0} \approx 1.2$ ms, indicating a strong depletion of interfacial vorticity within the 0–$5/k$ region. Thereafter, $\Gamma_{interface}$ remains nearly constant at a low level of approximately $0.25\ \mathrm{m^2\ s^{-1}}$, which is even much lower than the corresponding value for case 2-40 ($\approx 0.4\ \mathrm{m^2\ s^{-1}}$). As a result, the interfacial vorticity within the 0–$5/k$ region remains insufficient to sustain the high bubble velocity, leading to continuous deceleration.

https://doi.org/10.1017/jfm.2026.11898 Published online by Cambridge University Press

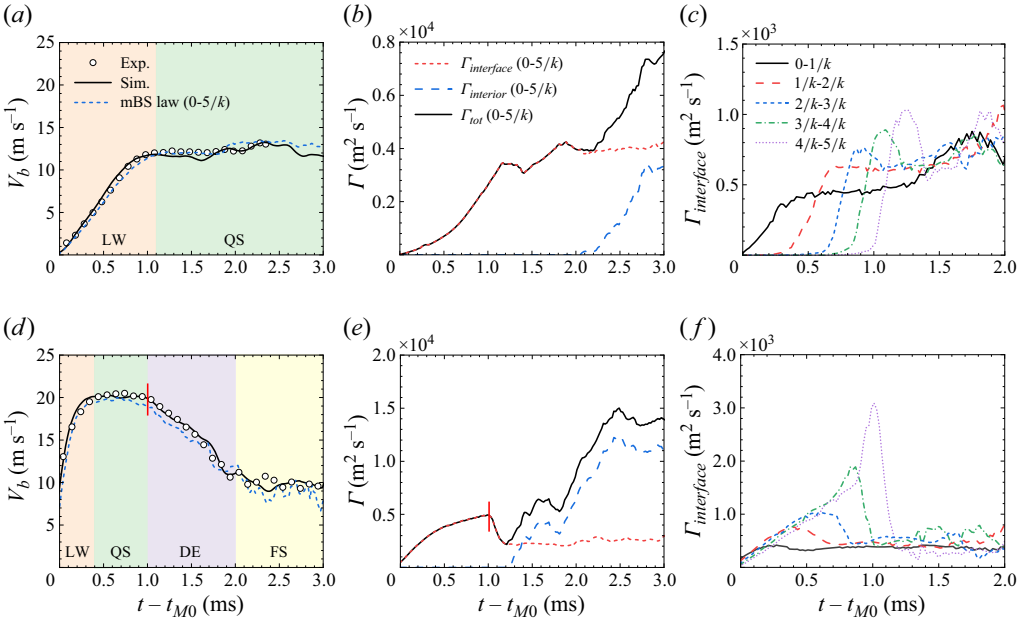


Figure 11. Temporal evolution of bubble velocity and its associated area-integrated vorticity for cases 2-40 (*a–c*) and 20-40 (*d–f*). The modified BS law extends the BS framework by incorporating the stretching effect induced by the bulk velocity difference. In panels (*d*, *e*), the vertical red lines at $t - t_{M0} = 1.0$ ms highlight the temporal correspondence between the onset of bubble deceleration and the reduction of interfacial vorticity within the 0–5/k region.

The value of $\Gamma_{interior}$ in case 20-40 increases rapidly after $t - t_{M0} \approx 1.2$ ms and approaches saturation by $t - t_{M0} \approx 1.7$ ms (see figure 11*e*). Although the rapid increase of $\Gamma_{interior}$ raises Γ_{tot} to approximately 1.5 m^2 s^{-1}, nearly six times the corresponding value of $\Gamma_{interface}$, the decreasing trend of V_b shown in figure 11(*d*) is still unchanged before $t - t_{M0} \approx 2.5$ ms. This further indicates that the shed vortices exert only a very limited influence on bubble growth, despite entering the 0–5/k region. The weak contribution of these interior vortices arises primarily from their location almost directly beneath the bubble tip, so that the induced vertical velocity at the bubble tip is small. In addition, the disordered nature of the interior vorticity field leads to non-constructive interference, resulting in substantial cancellation of the induced velocity. It is noteworthy that the decrease of V_b ceases at approximately $t - t_{M0} \approx 2.5$ ms. At this time, as shown in figure 10(*j*), the shed vortices have reached the bubble tip. Their close proximity enables the induced velocity to become significant, ultimately terminating the bubble deceleration and leading to fluctuating saturated bubble growth.

To further elucidate the distinct evolution of interfacial vorticity under low- and high-amplitude conditions, figures 11(*c*) and 11(*f*) present the temporal evolution of $\Gamma_{interface}$ within the 0–1/k, 1/k-2/k, 2/k-3/k, 3/k-4/k and 4/k-5/k subregions for cases 2-40 and 20-40, respectively. For case 2-40, the streamwise extent of the interface is initially less than 1/k. Consequently, as shown in figure 11(*c*), except for the 0–1/k subregion, $\Gamma_{interface}$ in the remaining subregions does not increase from the initial time, but instead begins to rise sequentially as the interface extends into the corresponding subregions. Overall, despite slight decrease in $\Gamma_{interface}$ for the three subregions between 2/k and 5/k, $\Gamma_{interface}$ consistently maintains relatively high levels and tends to converge at late times. For case

https://doi.org/10.1017/jfm.2026.11898 Published online by Cambridge University Press

20-40, except for the 0–1/k region which contains only a small amount of vorticity, the decrease of $\Gamma_{interface}$ in each upstream subregion is accompanied by a comparable increase in the adjacent downstream subregion, as shown in figure 11(f). This nearly conservative transfer indicates a progressive downstream advection of interfacial vorticity. As a result, $\Gamma_{interface}$ in all subregions within the 0–5/k region decays to very low levels at late times. This downstream transport is driven by a 'pump-like' effect induced by the KH vortices along the spike. As the initial amplitude increases, these KH vortices become stronger and more effective in advecting interfacial vorticity away from the bubble region toward the spike (see figure 10h), which leads to a progressive depletion of vorticity in the bubble vicinity and consequently suppressing bubble growth.

In short, under low-amplitude conditions, both stretching and curvature effects remain weak, and bubble growth reaches a quasi-steady state primarily governed by inertial effects, whose long-term persistence is supported by sufficient interfacial vorticity remaining in the near-tip region. In contrast, under high-amplitude conditions, the inertial effect provides the fundamental contribution to bubble growth, whereas the curvature effect governs the transition to the quasi-steady state and the stretching effect determines the magnitude of the quasi-steady velocity. Beyond the quasi-steady stage, strong KH vortices along the spike continuously extract interfacial vorticity from the bubble region and transport it downstream toward the spike. This weakens the interfacial vorticity that sustains bubble motion, thereby causing continuous bubble deceleration. As the vortices shed from the spike reach the vicinity of the bubble tip, their induced velocity becomes significant, eventually terminating the deceleration and leading to a fluctuating saturated state.

3.5. *Discussion*

This subsection discusses the underlying reason for the inability of the present model (3.29) to predict the bubble growth in the deceleration stage, followed by potential directions for future improvements. The present model is developed within the classical Layzer-type potential-flow framework, in which the bubble dynamics is governed solely by bubble-front distortion (i.e. the evolution of bubble curvature) (Goncharov 2002; Abarzhi *et al.* 2003*a*; Abarzhi *et al.* 2003*b*; Liu *et al.* 2023*b*). Under high-amplitude conditions, however, vorticity transport from the bubble region toward the spike is evident, leading to a continuous reduction in bubble velocity. This indicates that the bubble dynamics is governed not only by bubble-front distortion but also strongly by the evolving vorticity field. Since the present model does not incorporate the dynamic redistribution of vorticity, it fails to capture the late-time bubble behaviour at high amplitudes.

Future theoretical developments should therefore incorporate vorticity transport into the potential-flow description as an additional dynamic effect. In this regard, the group-theory framework developed by Abarzhi and co-workers (Abarzhi *et al.* 2003*a*; Abarzhi *et al.* 2003*b*; Abarzhi *et al.* 2015; Abarzhi *et al.* 2023; Abarzhi 2024) provides a promising direction. Unlike traditional Layzer-type models, which rely on local expansions near the bubble tip, the group-theory approach describes coherent nonlinear structures through symmetry-based representations of the global flow field. Such a framework provides a more suitable basis for extending the present theory beyond the purely potential-flow approximation and for incorporating additional physics, such as interfacial shear and vortical transport. For the high-amplitude interface with strongly vorticity redistribution, a group-theory-based approach is believed to offer improved robustness in describing the late-time RTI bubble evolution.

https://doi.org/10.1017/jfm.2026.11898 Published online by Cambridge University Press

4. Conclusion

The evolution of rarefaction-driven RTI at high-amplitude, single-mode interfaces is investigated, focusing on the finger dynamics. In contrast to RTI driven by gravity or mechanical acceleration, rarefaction-driven RTI features a distinct WT stage prior to the linear stage, and the WT-stage influence becomes increasingly prominent as the amplitude–wavelength ratio (η_0/λ) increases. The finger velocities in the WT stage can be decoupled into two components: bulk motion induced by the rarefaction flow and velocity induced by baroclinic vorticity. The bulk contribution dominates the entire WT stage for spikes, but for bubbles, it prevails only at low amplitudes (low η_0/λ). At higher η_0/λ values, the vorticity contribution takes over and becomes dominant by the end of the WT stage. By integrating a 1-D rarefaction-flow theory with a vorticity-based model, we quantitatively evaluate the respective contributions of bulk motion and vorticity. This analysis yields finger velocities that are in close agreement with numerical simulations.

At high amplitudes, the linear phase is brief and finger evolution rapidly becomes nonlinear. Incorporating the finger velocity and amplitude obtained from the WT stage into the Layzer-type model (Li *et al.* 2025), effectively avoids the singularity-induced ill posedness that occurs under high-amplitude conditions. As the interface stretching due to the bulk velocity difference between the bubble and spike tips becomes pronounced, its inclusion allows the Layzer-type model to accurately predict the perturbation growth across the linear-to-weakly nonlinear and quasi-steady stages.

Under low-amplitude conditions, bubble growth reaches a quasi-steady state primarily governed by inertial effects, which are sustained by sufficient interfacial vorticity retained in the near-tip region. In contrast, under high-amplitude conditions, the inertial effect provides the fundamental contribution to bubble growth, whereas the curvature effect governs the transition to the quasi-steady state and the stretching effect determines the magnitude of the quasi-steady velocity. Beyond the quasi-steady stage, bubble evolution at high amplitudes exhibits two additional stages: deceleration and fluctuating saturation. The deceleration originates from strong vorticity transport from the bubble region toward the spike, driven by KH vortices along the spike. This transport reduces the interfacial vorticity that sustains bubble motion and thus leads to growth suppression. As the vortices shed from the spike reach the vicinity of the bubble tip, their induced velocity becomes significant, eventually terminating the deceleration and leading to a fluctuating saturated state.

Future work will focus on developing theoretical descriptions for late-time bubble evolution at high amplitudes, where the effects of vorticity transport become increasingly important. In this regard, the group-theory framework developed by Abarzhi and collaborators (Abarzhi *et al.* 2003*b*; Abarzhi *et al.* 2015; Abarzhi *et al.* 2023; Abarzhi 2024) may provide a promising pathway for modelling the high-amplitude rarefaction-driven bubble dynamics.

Acknowledgements. The authors would like to thank Dr Z. Zhou for his help in numerical simulations.

Funding. This work was supported by the National Natural Science Foundation of China (nos. 12302371, 12372281 and 12388101), the Strategic Priority Research Program of Chinese Academy of Sciences (no. XDB0620201).

Declaration of interests. The authors report no conflict of interest.

https://doi.org/10.1017/jfm.2026.11898 Published online by Cambridge University Press

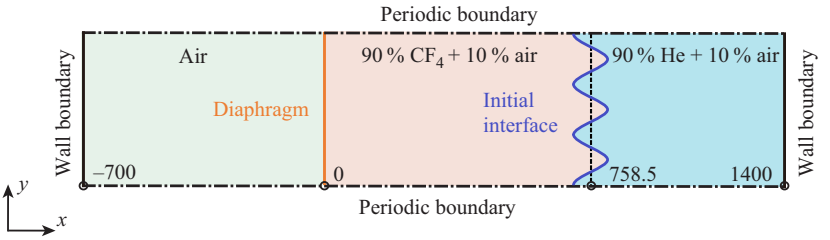


Figure 12. The computational domain used for the rarefaction–interface interaction. The numbers indicate spatial locations in millimetres.

Appendix A. Numerical methods

The rarefaction-driven single-mode RTI is modelled by solving the 2-D compressible multi-component Euler equations. To accurately resolve the fine-scale interface structures, an optimised six-point weighted compact nonlinear scheme (WCNS) with state-of-the-art spectral properties (Zhou *et al.* 2023*b*) is employed. The enhancement of this scheme involves a threefold strategy: (i) the approximated dispersion relation technique (Pirozzoli 2006) is utilised to optimise two free parameters, aligning the nonlinear scheme's performance with spectral-like accuracy; (ii) an advanced nonlinear weighting function proposed by Wong & Lele (2017) is incorporated, with its key parameter C optimised for improved spectral performance; (iii) the optimised parameters are dynamically adjusted at each grid point based on local flow physics to facilitate adaptive dissipation. This comprehensive optimisation yields a refined WCNS formulation with both minimal dispersion and flow-dependent dissipation. By incorporating the double-flux algorithm of Abgrall & Karni (2001), the WCNS is then extended to multi-species flows, and has demonstrated robust performance in simulating RTI and shock-driven interface instabilities (Zhou *et al.* 2023*a*, 2024; Li *et al.* 2025). Further details about the WCNS scheme can be found in Zhou *et al.* (2023*b*).

The simulations are performed in a 2-D rectangular computational domain of $2100 \times 120\ \text{mm}^2$, as shown in figure 12. The virtual diaphragm is placed at $x = 0$, and the initial interface is located at $x = 758.5$ mm. The left and right boundaries are set at $x = -700$ and 1400 mm, respectively, where wall boundary conditions are imposed, while periodic boundary conditions are applied in the transverse direction. The gas compositions on both sides of the interface are identical to those in the experiments. A pressure discontinuity is imposed across $x = 0$, generating rarefaction waves propagating in the positive x-direction.

In our previous study on small-amplitude single-mode RTI driven by rarefaction waves, grid-convergence tests were performed using four mesh sizes (0.5, 0.4, 0.2 and 0.1 mm) (Li *et al.* 2025). The results showed clear convergence with mesh refinement, with the 0.2 mm grid yielding results very close to those obtained using the 0.1 mm grid. Following the previous work (Li *et al.* 2025), a mesh size of 0.2 mm is selected in the present simulations to balance computational cost and accuracy. In addition, the agreement between numerical and experimental results for small-amplitude cases has already been validated in that work (Li *et al.* 2025). To further assess the numerical approach under high-amplitude conditions, figure 13 compares the schlieren images of interface evolution (panels (a, b)) and the temporal evolution of interface amplitude (panel (c)) for case 20-40 between experimental and numerical results, again showing good agreement.

https://doi.org/10.1017/jfm.2026.11898 Published online by Cambridge University Press

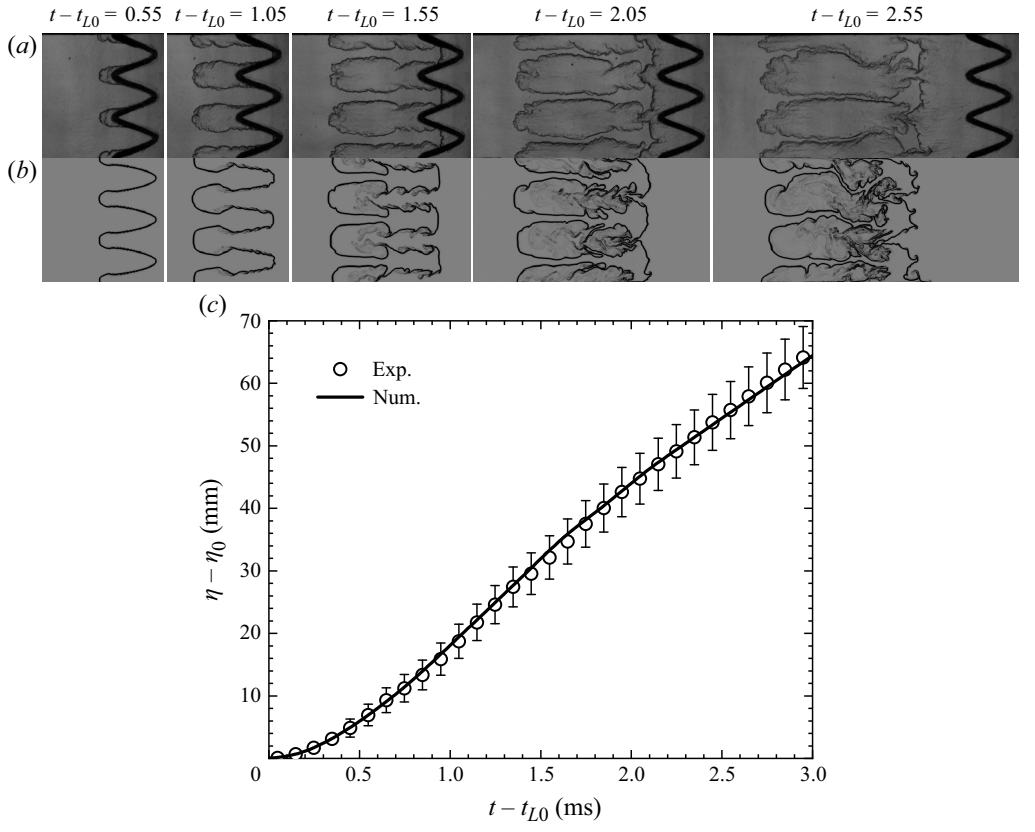


Figure 13. Qualitative and quantitative comparisons between experimental and numerical results for case 20-40: schlieren images of interface evolution from experiments (a) and simulations (b), and temporal evolution of perturbation amplitude (c). The unit of time in panels (a, b) is ms.

Appendix B. Determination of $C_{\rho R}$, C_{pR}, $C_{\rho L}$ and C_{pL}

In the rarefaction field, the dimensionless density and pressure distributions on both sides of the interface can be expressed through the isentropic relations (Han & Yin 1993)

$$C_{\rho R} = \frac{\rho_R}{\rho_{R0}} = \left(\frac{c_R}{c_{R0}}\right)^{\frac{2}{\gamma_R - 1}}, \quad C_{pR} = \frac{p_R}{p_{R0}} = \left(\frac{c_R}{c_{R0}}\right)^{\frac{2\gamma_R}{\gamma_R - 1}}, \tag{B1a}$$

$$C_{\rho L} = \frac{\rho_L}{\rho_{L0}} = \left(\frac{c_L}{c_{L0}}\right)^{\frac{2}{\gamma_L - 1}}, \quad C_{pL} = \frac{p_L}{p_{L0}} = \left(\frac{c_L}{c_{L0}}\right)^{\frac{2\gamma_L}{\gamma_L - 1}}, \tag{B1b}$$

where c_R and c_L denote the instantaneous sound speeds in the downstream and upstream regions, respectively.

In the downstream region of the interface, the flow field is governed by the simple wave relations

$$x = (u + c)t + f_1(u), \tag{B2a}$$

$$u - \frac{2}{\gamma_R - 1}c = K_1, \tag{B2b}$$

https://doi.org/10.1017/jfm.2026.11898 Published online by Cambridge University Press

where u, x and c denote the local flow velocity, location and sound speed, respectively. The function $f_1(u)$ is prescribed by the interface motion, while K_1 is a Riemann invariant. Evaluating (B2*b*) at the TRF ($u = 0$, $c = c_{R0}$) gives

$$K_1 = -\frac{2}{\gamma_R - 1} c_{R0}, \tag{B3}$$

so that within the TRW

$$c_R = c_{R0} + \frac{\gamma_R - 1}{2} u_R. \tag{B4}$$

At the interface $(x^{bulk}(t), u^{bulk}(t))$, (B2*a*) is satisfied, which allows elimination of $f_1(u)$

$$x - x^{bulk}(t) = \left[\left(c_{R0} + \frac{\gamma_R + 1}{2} u_R \right) - \left(c_{R0} + \frac{\gamma_R + 1}{2} u^{bulk}(t) \right) \right] t. \tag{B5}$$

Substituting (B4) into (B5) and rearranging yields

$$u_R = \frac{2}{\gamma_R + 1} \frac{x - x^{bulk}(t)}{t} + u^{bulk}(t), \tag{B6}$$

and therefore

$$\frac{c_R}{c_{R0}} = 1 + \frac{\gamma_R - 1}{2} \frac{\dfrac{2}{\gamma_R + 1} \dfrac{x - x^{bulk}(t)}{t} + u^{bulk}(t)}{c_{R0}}. \tag{B7}$$

Substituting (B7) into the isentropic relations (B1*a*) yields

$$C_{\rho R} = \left[1 + \frac{\gamma_R - 1}{2} \frac{\dfrac{2}{\gamma_R + 1} \dfrac{x - x^{bulk}(t)}{t} + u^{bulk}(t)}{c_{R0}} \right]^{\frac{2}{\gamma_R - 1}}, \tag{B8a}$$

$$C_{pR} = \left[1 + \frac{\gamma_R - 1}{2} \frac{\dfrac{2}{\gamma_R + 1} \dfrac{x - x^{bulk}(t)}{t} + u^{bulk}(t)}{c_{R0}} \right]^{\frac{2\gamma_R}{\gamma_R - 1}}. \tag{B8b}$$

The upstream side of the interface features a double-wave region, which consists of an IRW and a RCW. For the IRW, the flow satisfies

$$x = (u + c)t, \tag{B9a}$$

$$u - \frac{2}{\gamma_L - 1} c = K_2. \tag{B9b}$$

An intermediate point (x, u^*) is defined to represent the state affected only by the IRW but not yet influenced by the reflected wave. Given that both the intermediate state (x, u^*) and the state at the IRF ($u = 0$, $c = c_{L0}$) satisfy (B9*a*) and (B9*b*), the following relation can be obtained:

$$\frac{c^*}{c_{L0}} = 1 + \frac{\gamma_L - 1}{2} \frac{u^*}{c_{L0}}, \tag{B10}$$

https://doi.org/10.1017/jfm.2026.11898 Published online by Cambridge University Press

where

$$u^* = \left(\frac{x}{t} - c_{L0}\right)\frac{2}{\gamma_L + 1}. \tag{B11}$$

For the RCW, the flow satisfies

$$x = (u - c)t + f_2(u), \tag{B12a}$$

$$u + \frac{2}{\gamma_L - 1}c = K_3, \tag{B12b}$$

where $f_2(u)$ is determined by the interface motion in the reflected wave. Since both the interface state $(x^{bulk}(t), u^{bulk}(t))$ and the intermediate state (u^*, c^*) satisfy (B12*a*) and (B12*b*), the following relation holds:

$$\frac{c_L}{c^*} = 1 + \frac{\gamma_L - 1}{2}\frac{u^* - u_L}{c^*}, \tag{B13}$$

where

$$u_L = \frac{2}{\gamma_L + 1}\frac{x - x^{bulk}(t)}{t} + u^{bulk}(t) \tag{B14}$$

represents the local flow velocity within the reflected wave at any point. Finally, the dimensionless density and pressure distributions on the upstream side of the interface can be expressed as

$$C_{\rho L} = \left(\frac{c_L}{c^*}\frac{c^*}{c_{L0}}\right)^{\frac{2}{\gamma_L - 1}} = \left[\left(1 + \frac{\gamma_L - 1}{2}\frac{u^*}{c_{L0}}\right)\left(1 + \frac{\gamma_L - 1}{2}\frac{u^* - u_L}{c^*}\right)\right]^{\frac{2}{\gamma_L - 1}}, \tag{B15a}$$

$$C_{pL} = \left(\frac{c_L}{c^*}\frac{c^*}{c_{L0}}\right)^{\frac{2}{\gamma_L - 1}} = \left[\left(1 + \frac{\gamma_L - 1}{2}\frac{u^*}{c_{L0}}\right)\left(1 + \frac{\gamma_L - 1}{2}\frac{u^* - u_L}{c^*}\right)\right]^{\frac{2\gamma_L}{\gamma_L - 1}}. \tag{B15b}$$

References

Abarzhi, S.I. 2024 Perspective: group theory analysis and special self-similarity classes in Rayleigh–Taylor and Richtmyer–Meshkov interfacial mixing with variable accelerations. *Rev. Mod. Plasma Phys.* **8**, 15.

Abarzhi, S.I., Bhowmick, A.K., Naveh, A., Pandian, A., Swisher, N.C., Stellingwerf, R.F. & Arnett, W.D. 2019*a* Supernova, nuclear synthesis, fluid instabilities, and interfacial mixing. *Proc. Natl Acad. Sci. USA* **116**, 18184.

Abarzhi, S.I., Fukumoto, Y. & Kadanoff, L.P. 2015 Stability of a hydrodynamic discontinuity. *Phys. Scr.* **90**, 018002.

Abarzhi, S.I., Glimm, J. & Lin, A.D. 2003*a* Dynamics of two-dimensional Rayleigh–Taylor bubbles for fluids with a finite density contrast. *Phys. Fluids* **15**, 2190.

Abarzhi, S.I., Hill, D.L., Williams, K.C., Li, J.T. & Remington, B.A. 2023 Fluid dynamic mathematical aspects of supernova remnants. *Phys. Fluids* **35**, 034106.

Abarzhi, S.I., Ilyin, D.V., Goddard, W.A. & Anisimov, S.I. 2019*b* Interface dynamics: mechanisms of stabilization and destabilization and structure of flow fields. *Proc. Natl Acad. Sci. USA* **116**, 18218.

Abarzhi, S.I., Nishihara, K. & Glimm, J. 2003*b* Rayleigh–Taylor and Richtmyer–Meshkov instabilities for fluids with a finite density ratio. *Phys. Lett. A* **317**, 470–476.

Abarzhi, S.I. & Sreenivasan, K.R. 2010 Turbulent mixing and beyond. *Phil. Trans. R. Soc. Lond. A* **368**, 1539–1546.

Abgrall, R. & Karni, S. 2001 Computations of compressible multifluids. *J. Comput. Phys.* **169**, 594–623.

Akula, B., Suchandra, P., Mikhaeil, M. & Ranjan, D. 2017 Dynamics of unstably stratified free shear flows: an experimental investigation of coupled Kelvin–Helmholtz and Rayleigh–Taylor instability. *J. Fluid Mech.* **816**, 619–660.

https://doi.org/10.1017/jfm.2026.11898 Published online by Cambridge University Press

ANDREWS, M.J. & DALZIEL, S.B. 2010 Small Atwood number Rayleigh–Taylor experiments. *Phil. Trans. R. Soc. Lond. A* **368**, 1663–1679.
BANERJEE, A. 2020 Rayleigh–Taylor instability: a status review of experimental designs and measurement diagnostics. *J. Fluids Engng* **142**, 120801.
BANERJEE, A. & ANDREWS, M.J. 2006 Statistically steady measurements of Rayleigh–Taylor mixing in a gas channel. *Phys. Fluids* **18**, 035107.
BANERJEE, A., KRAFT, W.N. & ANDREWS, M.J. 2010 Detailed measurements of a statistically steady Rayleigh–Taylor mixing layer from small to high Atwood numbers. *J. Fluid Mech.* **659**, 127–190.
BETTI, R. & SANZ, J. 2006 Bubble acceleration in the ablative Rayleigh–Taylor instability. *Phys. Rev. Lett.* **97**, 205002.
BIAN, X., ALUIE, H., ZHAO, D., ZHANG, H. & LIVESCU, D. 2020 Revisiting the late-time growth of single-mode Rayleigh–Taylor instability and the role of vorticity. *Phys. D* **403**, 132250.
BOFFETTA, G. & MAZZINO, A. 2017 Incompressible Rayleigh–Taylor turbulence. *Annu. Rev. Fluid Mech.* **49**, 119–143.
CHAN, W., JAIN, S.S., HWANG, H., NAVEH, A. & ABARZHI, S.I. 2023 Theory and simulations of linear and nonlinear two-dimensional Rayleigh–Taylor dynamics with variable acceleration. *Phys. Fluids* **35**, 059902.
CONG, Z., GUO, X., SI, T. & LUO, X. 2022 Experimental and theoretical studies on heavy fluid layers with reshock. *Phys. Fluids* **34**, 104108.
DIMONTE, G. et al. 1996 A linear electric motor to study turbulent hydrodynamics. *Rev. Sci. Instrum.* **67**, 302–306.
DIMONTE, G. & SCHNEIDER, M. 2000 Density ratio dependence of Rayleigh–Taylor mixing for sustained and impulsive acceleration histories. *Phys. Fluids* **12**, 304–321.
FU, C., ZHAO, Z., WANG, P., LIU, N., WAN, Z. & LU, X. 2023 Bubble re-acceleration behaviours in compressible Rayleigh–Taylor instability with isothermal stratification. *J. Fluid Mech.* **954**, A16.
GAO, X., GUO, X., ZHAI, Z. & LUO, X. 2024 Interfacial instabilities driven by co-directional rarefaction and shock waves. *J. Fluid Mech.* **980**, A20.
GONCHAROV, V.N. 2002 Analytical model of nonlinear, single-mode, classical Rayleigh–Taylor instability at arbitrary Atwood numbers. *Phys. Rev. Lett.* **88**, 134502.
GONCHAROV, V.N., SKUPSKY, S., BOEHLY, T.R., KNAUER, J.P., MCKENTY, P., SMALYUK, V.A., TOWN, R.P.J., GOTCHEV, O.V., BETTI, R. & MEYERHOFER, D.D. 2000 A model of laser imprinting. *Phys. Plasmas* **7**, 2062–2068.
GRÉA, B.-J. & BRIARD, A. 2023 Inferring the magnetic field from the Rayleigh–Taylor instability. *Astrophys. J.* **958**, 164.
GUO, W. & ZHANG, Q. 2020 Universality and scaling laws among fingers at Rayleigh–Taylor and Richtmyer–Meshkov unstable interfaces in different dimensions. *Phys. D* **403**, 132304.
GUO, X., CONG, Z., SI, T. & LUO, X. 2022 Shock-tube studies of single- and quasi-single-mode perturbation growth in Richtmyer–Meshkov flows with reshock. *J. Fluid Mech.* **941**, A65.
GUO, X., XU, Z. & ZHAI, Z. 2025 Rarefaction-induced Rayleigh–Taylor growth for a light gas layer. *Phys. Fluids* **37**, 096134.
HAN, Z. & YIN, X. 1993 *Shock Dynamics*. Kluwer Academic Publishers and Science Press.
HUANG, Z., DE LUCA, A., ATHERTON, T.J., BIRD, M., ROSENBLATT, C. & CARLES, P. 2007 Rayleigh–Taylor instability experiments with precise and arbitrary control of the initial interface shape. *Phys. Rev. Lett.* **99**, 204502.
JACOBS, J.W. & DALZIEL, S.B. 2005 Rayleigh–Taylor instability in complex stratifications. *J. Fluid Mech.* **542**, 251–279.
JACOBS, J.W. & SHEELEY, J.M. 1996 Experimental study of incompressible Richtmyer–Meshkov instability. *Phys. Fluids* **8**, 405–415.
KUCHERENKO, Y.A., BALABIN, S.I., ARDASHOVA, R.I., KOZELKOV, O.E., DULOV, A.V. & ROMANOV, I.A. 2003 Experimental study of the influence of the stabilizing properties of transitional layers on the turbulent mixing evolution. *Laser Part. Beams* **21**, 369–373.
KUCHERENKO, Y.A., BALABIN, S.I., CHERRET, R. & HAAS, J.F. 1997 Experimental investigation into inertial properties of Rayleigh–Taylor turbulence. *Laser Part. Beams* **15**, 25–31.
KURANZ, C.C., PARK, H.-S., HUNTINGTON, C.M., MILES, A.R., REMINGTON, B.A., PLEWA, T., TRANTHAM, M.R., ROBEY, H.F., SHVARTS, D. & SHIMONY, A. 2018 How high energy fluxes may affect Rayleigh–Taylor instability growth in young supernova remnants. *Nat. Commun.* **9**, 1–6.
LAWRIE, A.G.W. & DALZIEL, S.B. 2011 Rayleigh–Taylor mixing in an otherwise stable stratification. *J. Fluid Mech.* **688**, 507–527.
LAYZER, D. 1955 On the instability of superposed fluids in a gravitational field. *Astrophys. J.* **122**, 1–12.

https://doi.org/10.1017/jfm.2026.11898 Published online by Cambridge University Press

LI, C. & BOOK, D.L. 1991 Instability generated by acceleration due to rarefaction waves. *Phys. Rev. A* **43**, 3153.

LI, C., KAILASANATH, K. & BOOK, D.L. 1991 Mixing enhancement by expansion waves in supersonic flows of different densities. *Phys. Fluids* **3**, 1369.

LI, J., CAO, Q., WANG, H., ZHAI, Z. & LUO, X. 2023 New interface formation method for shock-interface interaction studies. *Exp. Fluids* **64**, 170.

LI, Y., GAO, X., GUO, X., ZHAI, Z. & LUO, X. 2025 Single-mode Rayleigh–Taylor instability in time-dependent rarefaction-driven flows. *J. Fluid Mech.* **1016**, A27.

LIANG, Y., ALKINDI, A., ALZEYOUDI, K., LIU, L., ALI, M. & MASMOUDI, N. 2024 Experimental investigation of three-dimensional Rayleigh–Taylor instability of a gaseous interface. *J. Fluid Mech.* **994**, A7.

LIEPMANN, H.W. & ROSHKO, A. 1957 *Elements of Gasdynamics*. John Wiley & Sons, Inc.

LIU, C., WANG, H., ZHANG, Y. & XIAO, Z. 2023*a* A decoupled mechanism of interface growth in single-mode hydrodynamic instabilities. *J. Fluid Mech.* **964**, A37.

LIU, C., WU-WANG, H., ZHANG, Y. & XIAO, Z. 2025 Prediction of long-time single-mode Rayleigh–Taylor bubble evolution: a rotational flow model. *J. Fluid Mech.* **1023**, A23.

LIU, C., ZHANG, Y. & XIAO, Z. 2023*b* A unified theoretical model for spatiotemporal development of Rayleigh–Taylor and Richtmyer–Meshkov fingers. *J. Fluid Mech.* **954**, A13.

LIU, L., LIANG, Y., DING, J., LIU, N. & LUO, X. 2018 An elaborate experiment on the single-mode Richtmyer–Meshkov instability. *J. Fluid Mech.* **853**, R2.

LIVESCU, D. 2020 Turbulence with large thermal and compositional density variations. *Annu. Rev. Fluid Mech.* **52**, 309–341.

MESHKOV, E.E. & ABARZHI, S.I. 2019 Group theory and jelly's experiment of Rayleigh–Taylor instability and Rayleigh–Taylor interfacial mixing. *Fluid Dyn. Res.* **51**, 065502.

MIKAELIAN, K.O. 1998 Analytic approach to nonlinear Rayleigh–Taylor and Richtmyer–Meshkov instabilities. *Phys. Rev. Lett.* **80**, 508–511.

MIKAELIAN, K.O. 2008 Limitations and failures of the Layzer model for hydrodynamic instabilities. *Phys. Rev. E* **78**, 015303.

MIKAELIAN, K.O. 2009 Reshocks, rarefactions, and the generalized Layzer model for hydrodynamic instabilities. *Phys. Fluids* **21**, 024103.

MIKAELIAN, K.O. 2014 Shock-induced interface instability in viscous fluids and metals. *Phys. Rev. E* **89**, 053009.

MORGAN, R.V., CABOT, W.H., GREENOUGH, J.A. & JACOBS, J.W. 2018 Rarefaction-driven Rayleigh–Taylor instability. Part 2. Experiments and simulations in the nonlinear regime. *J. Fluid Mech.* **838**, 320–355.

MORGAN, R.V., LIKHACHEV, O.A. & JACOBS, J.W. 2016 Rarefaction-driven Rayleigh–Taylor instability. Part 1. Diffuse-interface linear stability measurements and theory. *J. Fluid Mech.* **791**, 34–60.

PIROZZOLI, S. 2006 On the spectral properties of shock-capturing schemes. *J. Comput. Phys.* **219**, 489–497.

POUQUET, A. & MININNI, P.D. 2014 The interplay between helicity and rotation in turbulence: implications for scaling laws and small-scale dynamics. *Phil. Trans. R. Soc. Lond. A* **368**, 1635–1662.

QIAO, X. & LAN, K. 2021 Novel target designs to mitigate hydrodynamic instabilities growth in inertial confinement fusion. *Phys. Rev. Lett.* **126**, 185001.

RAMAPRABHU, P., DIMONTE, G., WOODWARD, P., FRYER, C., ROCKEFELLER, G., MUTHURAMAN, K., LIN, P.-H. & JAYARAJ, J. 2012 The late-time dynamics of the single-mode Rayleigh–Taylor instability. *Phys. Fluids* **24**, 074107.

RAMAPRABHU, P., DIMONTE, G., YOUNG, Y., CALDER, A.C. & FRYXELL, B. 2006 Limits of the potential flow approach to the single-mode Rayleigh–Taylor problem. *Phys. Rev. E* **74**, 066308.

RAMAPRABHU, P., KARKHANIS, V., BANERJEE, R., VARSHOCHI, H., KHAN, M. & LAWRIE, A.G.W. 2016 Evolution of the single-mode Rayleigh–Taylor instability under the influence of time-dependent accelerations. *Phys. Rev. E* **93**, 013118.

RAVID, A., CITRON, R.I. & JEANLOZ, R. 2021 Hydrodynamic instability at impact interfaces and planetary implications. *Nat. Commun.* **12**, 2104.

RAYLEIGH, L. 1883 Investigation of the character of the equilibrium of an incompressible heavy fluid of variable density. *Proc. Lond. Math. Soc.* **14**, 170–177.

READ, K.I. 1984 Experimental investigation of turbulent mixing by Rayleigh–Taylor instability. *Physica D* **12**, 45–58.

SOHN, S.I. 2003 Simple potential-flow model of Rayleigh–Taylor and Richtmyer–Meshkov instabilities for all density ratios. *Phys. Rev. E* **67**, 026301.

https://doi.org/10.1017/jfm.2026.11898 Published online by Cambridge University Press

TAYLOR, G. 1950 The instability of liquid surfaces when accelerated in a direction perpendicular to their planes. I. *Proc. R. Soc. Lond. A* **201**, 192–196.
URZAY, J. 2018 Supersonic combustion in air-breathing propulsion systems for hypersonic flight. *Annu. Rev. Fluid Mech.* **50**, 593–627.
WANG, H., WANG, H., ZHAI, Z. & LUO, X. 2022 Effects of obstacles on shock-induced perturbation growth. *Phys. Fluids* **34**, 086112.
WEI, T. & LIVESCU, D. 2012 Late-time quadratic growth in single-mode Rayleigh–Taylor instability. *Phys. Rev. E* **86**, 046405.
WHITE, J., OAKLEY, J., ANDERSON, M. & BONAZZA, R. 2010 Experimental measurements of the nonlinear Rayleigh–Taylor instability using a magnetorheological fluid. *Phys. Rev. E* **81**, 026303.
WHITHAM, G.B. 1974 *Linear and Nonlinear Waves*. John Wiley & Sons, Inc.
WILKINSON, J.P. & JACOBS, J.W. 2007 Experimental study of the single-mode three-dimensional Rayleigh–Taylor instability. *Phys. Fluids* **19**, 124102.
WONG, M.L. & LELE, S.K. 2017 High-order localized dissipation weighted compact nonlinear scheme for shock- and interface-capturing in compressible flows. *J. Comput. Phys.* **339**, 179–209.
YAN, R., BETTI, R., SANZ, J., ALUIE, H., LIU, B. & FRANK, A. 2016 Three-dimensional single-mode nonlinear ablative Rayleigh–Taylor instability. *Phys. Plasmas* **23**, 022701.
YAN, Z., CHEN, Z., LI, J., WANG, L., LI, Z., ZHANG, C., GE, F., WU, J. & ZHANG, W. 2025 Hydrodynamic instability growth of the fuel-ablator interface induced by rippled rarefaction waves in inertial confinement fusion implosion experiments. *Matt. Radiation Extremes* **10**, 057602.
YOUNGS, D.L. 1989 Modelling turbulent mixing by Rayleigh–Taylor instability. *Physica D* **37**, 270–287.
ZHAI, Z., GAO, X., LI, Y., GUO, X. & LUO, X. 2025 Manipulation of single-mode perturbation growth driven by co-directional rarefaction and shock waves. *J. Fluid Mech.* **1015**, A36.
ZHANG, D., JIANG, X., TAO, T., LI, J., YAN, R., SUN, D. & ZHENG, J. 2024 Self-generated magnetic field in three-dimensional ablative Rayleigh–Taylor instability. *J. Fluid Mech.* **1000**, A94.
ZHANG, Q. 1998 Analytical solutions of Layzer-type approach to unstable interfacial fluid mixing. *Phys. Rev. Lett.* **81**, 3391.
ZHANG, Q. & GUO, W. 2016 Universality of finger growth in two-dimensional Rayleigh–Taylor and Richtmyer–Meshkov instabilities with all density ratios. *J. Fluid Mech.* **786**, 47–61.
ZHOU, Y. 2017*a* Rayleigh–Taylor and Richtmyer–Meshkov instability induced flow, turbulence, and mixing. I. *Phys. Rep.* **720–722**, 1–136.
ZHOU, Y. 2017*b* Rayleigh–Taylor and Richtmyer–Meshkov instability induced flow, turbulence, and mixing. II. *Phys. Rep.* **723–725**, 1–160.
ZHOU, Y., CLARK, T.T., CLARK, D.S., GLENDINNING, S.G., SKINNER, M.A., HUNTINGTON, C.M., HURRICANE, O.A., DIMITS, A.M. & REMINGTON, B.A. 2019 Turbulent mixing and transition criteria of flows induced by hydrodynamic instabilities. *Phys. Plasmas* **26**, 080901.
ZHOU, Y., SADLER, J.D. & HURRICANE, O.A. 2025 Instabilities and mixing in inertial confinement fusion. *Annu. Rev. Fluid Mech.* **57**, 197–225.
ZHOU, Y. *et al.* 2021 Rayleigh–Taylor and Richtmyer–Meshkov instabilities: a journey through scales. *Physica D* **423**, 132838.
ZHOU, Z., DING, J. & CHENG, W. 2024 Mixing and inter-scale energy transfer in Richtmyer–Meshkov turbulence. *J. Fluid Mech.* **984**, A56.
ZHOU, Z., DING, J., CHENG, W. & LUO, X. 2023*a* Scaling law of structure function of Richtmyer–Meshkov turbulence. *J. Fluid Mech.* **972**, A18.
ZHOU, Z., DING, J., HUANG, S. & LUO, X. 2023*b* A new type of weighted compact nonlinear scheme with minimum dispersion and adaptive dissipation for compressible flows. *Comput. Fluids* **262**, 105934.

https://doi.org/10.1017/jfm.2026.11898 Published online by Cambridge University Press